Journal of Materials Chemistry A

ROYAL SOCIETY OF CHEMISTRY

PAPER

View Article Online
View Journal | View Issue

Check for updates

Cite this: J. Mater. Chem. A, 2024, 12, 8543

Engineering of a hierarchical S-scheme 2D/3D heterojunction with graphdiyne (g-C_nH_{2n-2}) coated 3D porous $CoAl_2O_4$ nanoflowers for highly efficient photocatalytic H_2 evolution†

Xuqiang Hao, ‡* Wei Deng,‡ Yu Fan* and Zhiliang Jin *

Solar photocatalytic hydrolysis of hydrogen is one of the most important ways to solve energy and environmental problems. Rational design and modulation of interfaces in S-scheme heterojunctions still present significant challenges for solar hydrogen production. Herein, a novel 2D/3D hierarchical graphdiyne/$CoAl_2O_4$ (GCA) S-scheme heterojunction was successfully constructed by coupling graphdiyne (GDY) nanosheets onto porous $CoAl_2O_4$ nanoflowers. GDY was synthesized by a cross-coupling reaction and ultrathin 3D porous $CoAl_2O_4$ nanoflowers were transformed from CoAl-LDH. This unique 3D hierarchical porous structure of $CoAl_2O_4$ nanoflowers not only provides a larger specific surface area, sufficient active sites and enhanced light harvesting, but also significantly reduces the aggregation of GDY. Notably, hierarchical GCA-15 shows an exceptional photocatalytic hydrogen production rate of 5009.28 μmol g^{-1} h^{-1} under visible-light irradiation, which was 4.78 times higher than that of pristine $CoAl_2O_4$. This excellent photocatalytic activity can be attributed to the synergistic effect of the formed S-scheme heterojunction between GDY and $CoAl_2O_4$ and the 2D/3D hierarchical architecture. *In situ* irradiated XPS, UPS and DFT unveil the S-scheme electron transfer for GDY/$CoAl_2O_4$. The work functions and charge density difference further indicate the electrons transferring from GDY to $CoAl_2O_4$. This work provided a simple strategy for designing and constructing hierarchical graphdiyne-based S-scheme heterostructures for photocatalytic hydrogen production.

Received 19th February 2024
Accepted 23rd February 2024

DOI: 10.1039/d4ta01140f

rsc.li/materials-a

Published on 26 2024. Downloaded on 31.01.2026 3:43:36.

1. Introduction

The effective utilization of solar energy through photocatalysis technology can address contemporary environmental issues and energy crises.[1] However, practical development faces significant challenges due to the low efficiency of single photocatalysts.[2] The low efficiency of a single photocatalyst primarily stems from the delicate balance between light absorption and redox capability.[3] Specifically, narrow bandgap photocatalysts necessitate broad spectrum absorption of solar light, whereas wider bandgap photocatalysts require additional energy to drive photocatalytic reactions.[4] Meanwhile, the rapid recombination of photogenerated electrons and holes due to strong coulombic forces is also a major challenge.[5] Furthermore, Zhang *et al.* took an energy dissipation perspective, delving deep into the inherent reasons for the low efficiency of individual photocatalysts by referencing the processes occurring in dye molecules after light absorption. Photogenerated electrons and holes undergo processes akin to those outlined in the Jablonski diagram. These decay processes, including vibrational relaxation, lead to energy losses, posing a challenge to achieving full 100% energy utilization.[6] In order to overcome these limitations and improve the photocatalytic activity of individual photocatalysts, a lot of research has been carried out in the fields of morphology control,[7] doping,[8] and heterostructure construction.[9] Among them, S-scheme heterojunction photocatalysts can establish an internal electric field (IEF), effectively combining two or more photocatalytic properties, enhancing the absorption and utilization of solar energy and achieving much higher directional transmission rates of photogenerated carriers.[10] This greatly enhances the efficiency of separating photogenerated carriers, thereby expediting the photocatalytic reaction process.[1,9] Therefore, the rational design and preparation of efficient and stable S-scheme heterojunction photocatalysts hold great significance for enhancing photocatalytic performance and advancing photocatalytic technology.

The development and application of carbon materials have consistently been a prominent subject of scientific research.[11] Emerging carbon materials encompass fullerenes,[12] carbon

School of Chemistry and Chemical Engineering, Ningxia Key Laboratory of Solar Chemical Conversion Technology, and Key Laboratory for Chemical Engineering and Technology, State Ethnic Affairs Commission, North Minzu University, Yinchuan 750021, P. R. China. E-mail: haoxuqiang@126.com; zl-jin@nun.edu.cn

† Electronic supplementary information (ESI) available. See DOI: https://doi.org/10.1039/d4ta01140f

‡ These authors contributed equally to this work.

Published on 26 2024. Downloaded on 31.01.2026 3:43:36.

nanotubes,[13] graphdiyne[1] *etc.* Compared to other carbon materials, initial research on GDY was primarily centered around theoretical calculations and simulations. In 2010, Li *et al.* first successfully synthesised a graphdiyne film on copper surfaces using hexadecynyl benzene, and the synthesis and functionalization of GDY were set in motion.[14] GDY represents a novel 2D carbon nanomaterial, composed of sp-C hybrid states or carbon–carbon triple bonds (C≡C) that arise from sp-hybridization.[9] In essence, the molecular configuration of GDY is defined using the bonds involving sp-C and sp^2-C hybrid states. This results in GDY exhibiting characteristics such as high conjugation, a linear structure, and the absence of *cis–trans* isomers in the sp-hybridized carbon bonds.[15] These properties make GDY possess uniform pores, with a pore size of 0.55 nanometers and a pore density of 2.5×10^{-6} μm^{-2}, an appropriate bandgap, a large surface area, and a multi-layered structure, among other distinctive features.[16] These characteristics facilitate the exposure of numerous active sites and provide space for molecular diffusion. Therefore, GDY has been extensively studied in the field of photocatalysis. GDY can be artificially synthesized, and it is easily amenable to doping and functionalization through chemical methods. This has spurred the active involvement of numerous researchers in the study of this novel carbon material. Recently, our team substituted CuI for copper foil in the synthesis of GDY and conducted research on the application of the synthesized GDY in S-scheme heterojunction photocatalysts, for example, GDY/g-C_3N_4-V_N,[15] ZIF-67@GDY/CuI[16] *etc.* These results strongly demonstrate the possibility of constructing S-scheme heterojunctions with GDY materials.

Recently, bifunctional semiconductor materials have become a hot research topic due to their unique physicochemical properties.[17] Among them, three-dimensional (3D) hierarchical structures consisting of nanoribbons, nanorods, nanosheets, *etc.* are usually considered potentially promising candidates for photocatalysts, because the assembly of their building blocks can generate a large number of micro/nanopores, which can facilitate the diffusion and transport of molecules therein, thus enhancing the photocatalytic activity. Therefore, the design and construction of novel semiconductor hierarchical structures are important for realizing efficient photocatalysts. Layered double hydroxides (LDHs) are a type of two-dimensional brucite-like material, with their interlayer region composed of various divalent and trivalent metal cations. Due to their advantages such as tunable band gaps, cost-effectiveness, and environmental friendliness, LDHs have garnered widespread attention in the field of heterogeneous catalysis.[18] Compared with other layered double hydroxides, CoAl-LDHs exhibit excellent hydrogen production performance in photocatalytic hydrogen evolution due to their content of Co^{2+} ions that can promote the rapid dissociation of water molecules, which leads to the release of H.[19] Nevertheless, the swift recombination of photogenerated charge carriers on CoAl-LDH surfaces significantly hampers their energy conversion efficiency, and the larger bandgap also limits their light response range to the ultraviolet region.[18] By calcination at temperatures above 500 °C, LDHs can be topologically transformed into a mixture of metal oxides and spinel, giving them even better stability, a suitable bandgap and superior optoelectronic properties.[18,19] It is important to highlight that the atoms in the spinel structure are densely packed and well-stabilized, leading to excellent thermal stability, which ensures that structural integrity and stability are maintained even at elevated temperatures. Lv *et al.* employed a thermal treatment method to convert thin 3D flower-like CoAl-layered double hydroxides into ultrathin flower-like 3D porous spinel $CoAl_2O_4$-750. These CoAl spinel catalysts demonstrate remarkable stability and enhance the efficiency of photocatalytic CO_2 reduction.[20] Furthermore, the microstructure of materials is closely related to their properties. Therefore, the design of 3D nanopore structures emerges as an effective approach to achieving the efficient separation of photogenerated charges and broadened absorption spectra.[9,18] In contrast to block or sheet structures, 3D macroporous structures exhibit a slow photon effect, capable of retarding and capturing incident light at specific wavelengths, thereby enhancing the light absorption efficiency of 3D materials.[21] Considering the advantages of three-dimensional hierarchical structures of $CoAl_2O_4$ nanoflowers with ultrathin nanosheets, a hierarchical S-scheme heterojunction was rationally designed by coupling $CoAl_2O_4$ with GDY nanosheets looking forward to achieve higher charge separation efficiency for photocatalytic water splitting.

Herein, we have successfully synthesized a novel hierarchical 2D/3D GDY/$CoAl_2O_4$ S-scheme heterojunction by coating 2D GDY nanosheets onto the 3D porous spinel $CoAl_2O_4$ nanoflowers through physical mixing. The microstructure of GDY/$CoAl_2O_4$, the charge transfer mode, *etc.* were explained in detail by specific characterization. In addition, the strong coupling interaction between GDY and $CoAl_2O_4$ was confirmed by density-functional theory calculations and *in situ* XPS and followed an S-scheme charge transfer pathway. Through careful optimization of the structure and precise control of the interface, the GCA-15 heterojunction exhibits exceptional photocatalytic H_2 evolution performance, which is 4.78 times higher compared to pure 3D porous $CoAl_2O_4$ nanoflowers under visible-light irradiation. This work not only provides insights into the design of an S-scheme heterojunction with a three-dimensional hierarchical structure, but also provides multifunctional materials for environmental and energy utilization.

2. Results and discussion

The synthesis process of the porous $CoAl_2O_4$ nanoflowers and 2D/3D GDY/$CoAl_2O_4$ heterojunction is shown in Fig. 1. The ultrathin nanosheet-assembled porous nanoflower microsphere $CoAl_2O_4$ hierarchical architecture was first prepared through a simple annealing method. $Co(NO_3)_2 \cdot 6H_2O$ and $Al(NO_3)_3 \cdot 9H_2O$ are employed as sources of Co^{2+} and Al^{3+} ions, respectively. Urea serves as a pH buffer and an antioxidation agent to prevent the oxidation of Co^{2+}.[20] The CoAl-LDH nanoflower are synthesized by heating the mixture at 90 °C for 5 h. Following that, calcination of CoAl-LDHs resulted in the formation of ultrathin porous $CoAl_2O_4$ nanoflowers. Importantly, GDY nanosheets were synthesized *via* a Glazer–Hay

 This journal is © The Royal Society of Chemistry 2024

Published on 26 2024. Downloaded on 31.01.2026 3:43:36.

Fig. 1 Schematic of the fabrication process for $CoAl_2O_4$ nanoflowers and the 2D/3D GDY/$CoAl_2O_4$ heterojunction.

coupling reaction employing CuI as the catalytic substrate (Fig. S1†). Finally, the hierarchical 2D/3D GDY/$CoAl_2O_4$ hybrids were obtained by coupling $CoAl_2O_4$ with varying proportions of GDY *via* physical mixing.

2.1 Structure and morphology analysis

X-ray diffraction (XRD) was used to analyze the bulk-phase structural characteristics of GDY, CoAl-LDHs, annealed porous $CoAl_2O_4$ nanoflowers and GCA-*X*. Fig. 2a shows a diffraction peak for pure GDY at 23°, characterized by its broad and weak nature, corresponding to the (002) crystal plane of the amorphous carbon material.[22] After calcination, the CoAl-LDHs underwent a transformation into a $CoAl_2O_4$ spinel structure (JCPDS no. 44-0160). Notably, four distinct peaks at 31.1°, 36.8°, 59.1°, and 65.0° correspond to the (220), (311), (511), and (440) diffraction planes, respectively.[23] Distinct characteristic peaks exclusive to $CoAl_2O_4$ were observed in the GCA-15 sample, indicating that the incorporation of GDY does not disrupt the crystalline structure of $CoAl_2O_4$. It's noteworthy that no characteristic peaks associated with GDY were detected in the GCA-15 sample, possibly due to the low loading of GDY and the relatively small diffraction peaks. Fig. 2b depicts XRD patterns of GCA-*X* composites with different GDY contents (10%, 15%, 20%, 25%, and 30%). All GCA-*X* samples exhibit similar diffraction peaks, and no additional peaks are observed across all composites, affirming the high purity of the catalysts.

Fourier transform infrared spectroscopy (FTIR) is utilized for spectral analysis of GDY, $CoAl_2O_4$, and GCA to determine the types of compounds and molecular structures present in the samples by analyzing the peak positions. As depicted in Fig. 3a, the observed vibrational peaks at 841 cm^{-1}, 1369 cm^{-1}, and

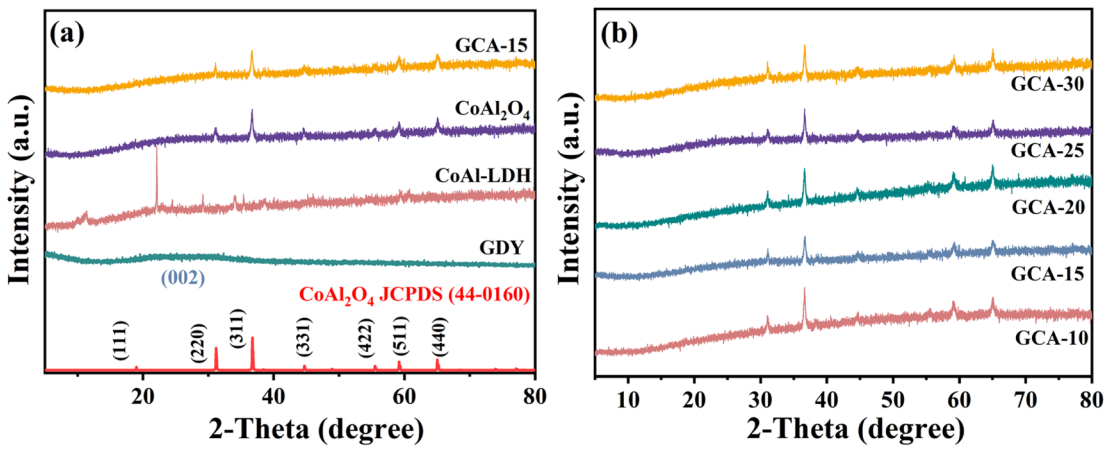

Fig. 2 (a) XRD patterns of GDY, precursor CoAl-LDHs, annealed $CoAl_2O_4$ and GCA-15; (b) GCA-*X* samples.

Published on 26 2024. Downloaded on 31.01.2026 3:43:36.

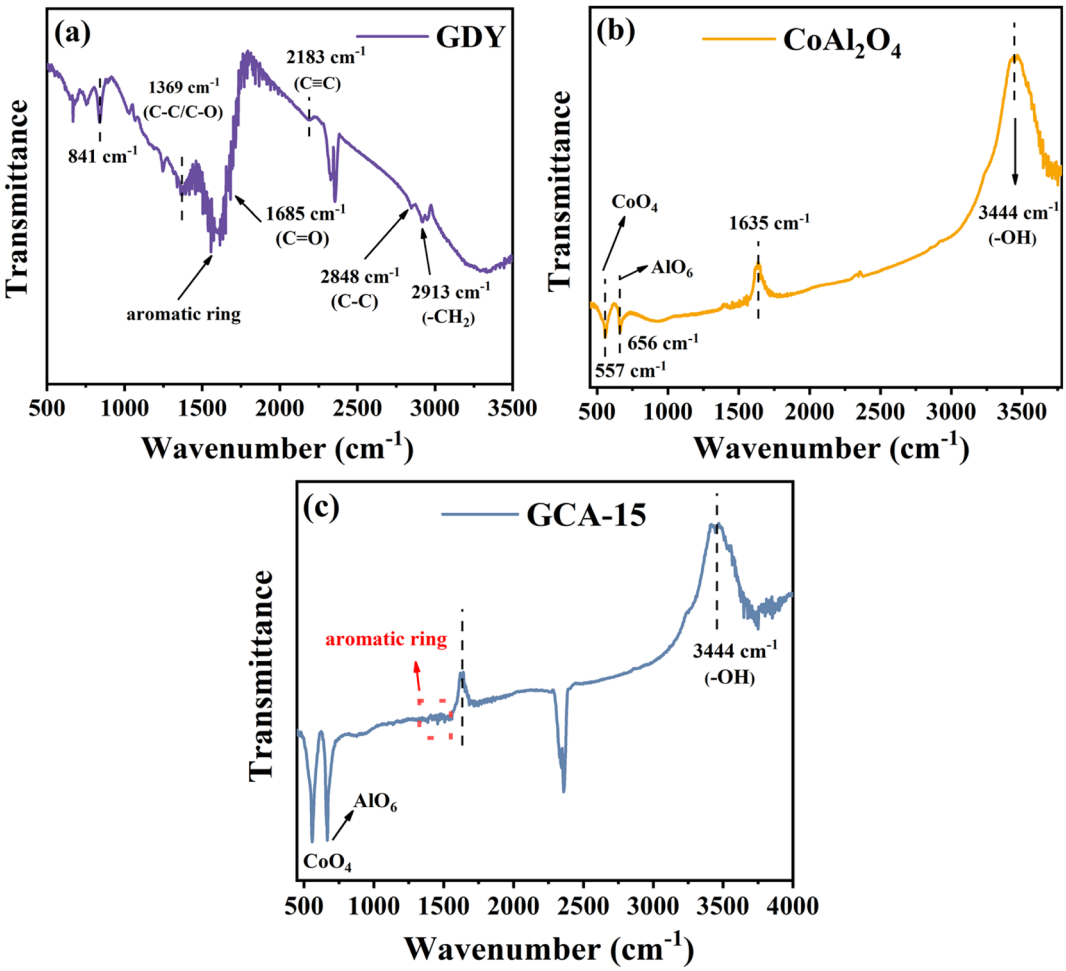

Fig. 3 FTIR spectra of (a) GDY, (b) $CoAl_2O_4$ and (c) GCA-15.

1595 cm^{-1} of the pure GDY sample originate from the stretching vibrations of C–C/C–O bonds and the skeletal vibrations of the aromatic ring.[24] The band located at 2183 cm^{-1} can be imputed to C≡C stretching vibrations, verifying the successful synthesis of GDY. These specific vibration frequency bands at 1685 cm^{-1}, 2848 cm^{-1}, and 2913 cm^{-1} correspond to the presence of C=O, C–C and $-CH_2$, respectively.[25] It's worth noting that the peak at 2358 cm^{-1} is due to the symmetric stretching vibration of carbon dioxide in the air.[14] To provide further insight into the bond types within GDY, a Raman test was performed (Fig. S2†). The Raman spectrum of GDY reveals distinct peaks at 1361 cm^{-1} and 1577 cm^{-1}. These peaks correspond to the first-order scattering of the E_{2g} mode, representing the in-phase stretching vibration of the sp^2 carbon lattice (referred to as the G band) within the aromatic ring and the vibrational motion of the sp^2 carbon domain (known as the D band). Furthermore, the peaks observed at 2039 cm^{-1} and 2175 cm^{-1} are attributed to the oscillations of the conjugated diacetylene chain (–C≡C–C≡C–).[16] These findings provide strong evidence for the successful synthesis of GDY.

In Fig. 3b, the FT-IR spectra of $CoAl_2O_4$ catalysts are presented. The stretching frequencies at approximately 700 cm^{-1} in the $CoAl_2O_4$ catalysts are attributed to vibrations related to M–O, Al–O, and M–O–Al bonds, with M representing either Al or Co.[18] The distinct peaks observed at approximately 557 cm^{-1} and 656 cm^{-1} are characteristic vibration modes of $CoAl_2O_4$. These vibrational bands correspond to the CoO_4 and AlO_6 units which constitute the $CoAl_2O_4$ structure, providing evidence that the transformation of CoAl-LDHs into spinel-structured $CoAl_2O_4$ occurs post-calcination.[19,20] The FT-IR results align with the findings from XRD analysis. In Fig. 3c, the distinctive aromatic ring peak specific to GDY is observed and the characteristic peak attributed to $CoAl_2O_4$ is also present. This observation result indicates that the introduction of GDY has not altered the inherent chemical bonds of $CoAl_2O_4$, further substantiating the successful synthesis of the GDY/$CoAl_2O_4$ sample.

Surface structures and morphologies of GDY, $CoAl_2O_4$ and GCA-15 were analyzed utilizing SEM and TEM. As illustrated in Fig. 4a, the synthesized GDY displays a clearly defined stacked lamellar structure with no apparent curling at the sheet edges. This observation underscores the uniformity and continuity of the GDY nanosheets.[16] Fig. 4b displays the SEM image of CoAl-LDHs, revealing a hierarchical 3D flower-like structure

 This journal is © The Royal Society of Chemistry 2024

Published on 26 2024. Downloaded on 31.01.2026 3:43:36.

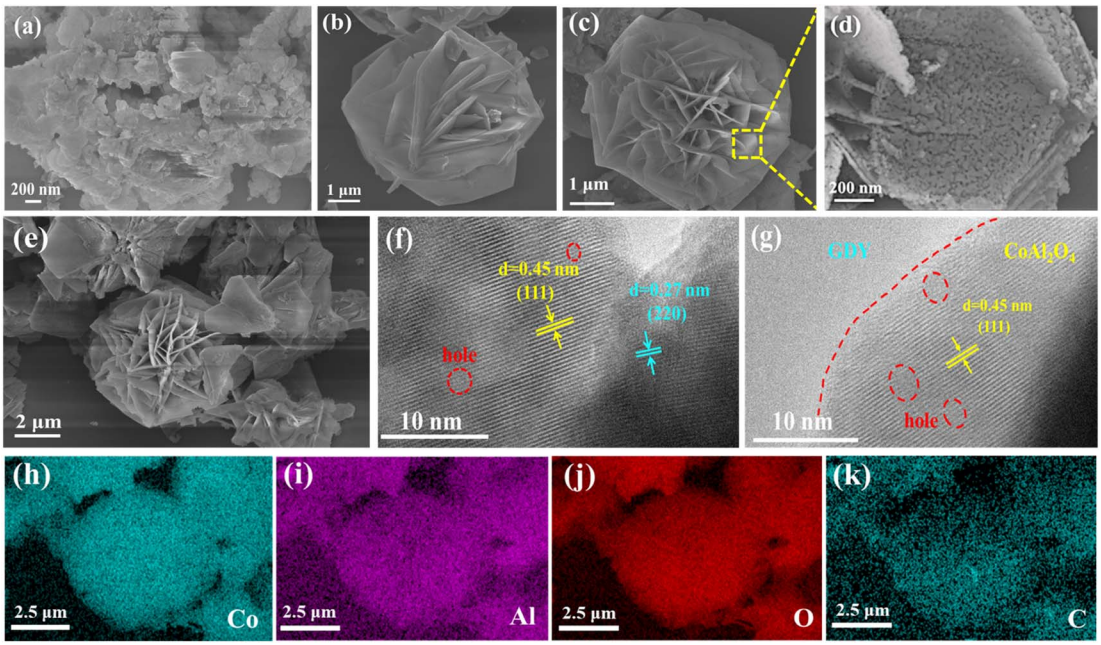

Fig. 4 SEM images of (a) GDY, (b) CoAl-LDHs, (c and d) $CoAl_2O_4$ and (e) GCA-15; HRTEM images of (f) $CoAl_2O_4$ and (g) GCA-15; elemental mappings (h–k) of the area in (e) for GCA-15.

characterized by 2D nanosheet petals. Even after the annealing process (as depicted in Fig. 4c), the formed $CoAl_2O_4$ structure continues to maintain the 3D flower-like hierarchical architecture of CoAl-LDHs (Fig. S3a–d†). Annealing also generates a considerable number of pores within the thinner 2D nanosheet petals (Fig. 4d). This nano-sized flower structure features numerous open spaces and a significantly expanded active surface area, contributing to the enhancement of photocatalytic performance.[20] Furthermore, Fig. S4† provides a more intuitive representation of the thickness changes in CoAl-LDH nanosheets after calcination. Post-calcination, the thickness of $CoAl_2O_4$ becomes thinner, which contributes to the faster facilitation of electron conduction.[20,26] From Fig. 4e and S3e, f,† it is obvious that GCA as a whole exhibits a flower-like shape, and the GDY nanosheets are dispersed on the surface of the nanoflower-like structure. Notably, the nanoflower structure retains its porous characteristics, indicating that during the physical stirring process, the overall morphology of the $CoAl_2O_4$ porous nanoflower is successfully integrated into GCA, and the introduction of GDY does not destroy its basic morphology. Furthermore, an in-depth analysis of the crystal structure and morphology of $CoAl_2O_4$ and GCA-15 was carried out using HRTEM. As shown in Fig. 4f, it is clear that there are two lattice spacings of 0.45 nm and 0.27 nm on $CoAl_2O_4$, corresponding to the (111) and (220) crystal planes, respectively. Additionally, the presence of pores is observed, highlighted by red dashed lines. As shown in Fig. 4g, the HRTEM image of GCA-15 displays distinct interface separation. The left side of the red dashed line exhibits an amorphous nature, consistent with the characteristics of GDY, while the right side matches the crystal structure observed in Fig. 4f, which is that of $CoAl_2O_4$. Consequently, it can be concluded that GDY is closely integrated with $CoAl_2O_4$. Furthermore, the elemental mapping structure (Fig. 4h–k) reveals the presence of four elements (Co, Al, O and C) in a uniform distribution within the GCA-15 sample, providing further confirmation of the successful synthesis of the GCA photocatalyst.

X-ray photoelectron spectroscopy (XPS) was employed to examine the atomic valence states and surface chemical composition of GDY, $CoAl_2O_4$, and GCA-15. It's essential to underscore that the robust coulombic attraction between the atom outer electrons and its nucleus has a profound impact on the element electron binding energy.[27] Simultaneously, an increase in an element binding energy indicates a decrease in electron density, resulting in electron loss from the atom. Conversely, a decrease in binding energy indicates an increase in electron density. Consequently, variations in binding energy directly influence the direction of carrier migration within the photocatalyst.[15] The high-resolution Co 2p XPS spectrum of $CoAl_2O_4$ (Fig. 5a) can be deconvoluted into two spin–orbit split components and two vibrational satellites. The binding energies for Co $2p_{3/2}$ and Co $2p_{1/2}$ in CoAl-LDHs are 779.31 eV and 794.48 eV, respectively. These values align with the XRD results, affirming the presence of Co^{2+} in the tetrahedral site within the $CoAl_2O_4$ spinel structure, where Co^{2+} is bonded to four equivalent O^{2-} atoms to create CoO_4 tetrahedra that share corners with twelve equivalent AlO_6 octahedra.[20,23,25] Simultaneously, Co^{3+} species are generated within $CoAl_2O_4$. The XPS spectra of Al 2p (Fig. 5b) reveal a singlet peak at a binding energy of 72.5 eV for $CoAl_2O_4$, which can be attributed to the presence of Al^{3+} ions occupying octahedral sites. These Al^{3+} ions are bonded to six equivalent O^{2-} atoms, forming AlO_6 octahedra that share corners with six equivalent CoO_4 tetrahedra and edges with six equivalent AlO_6 octahedra.[28] In the O 1s spectrum of $CoAl_2O_4$

Published on 26 2024. Downloaded on 31.01.2026 3:43:36.

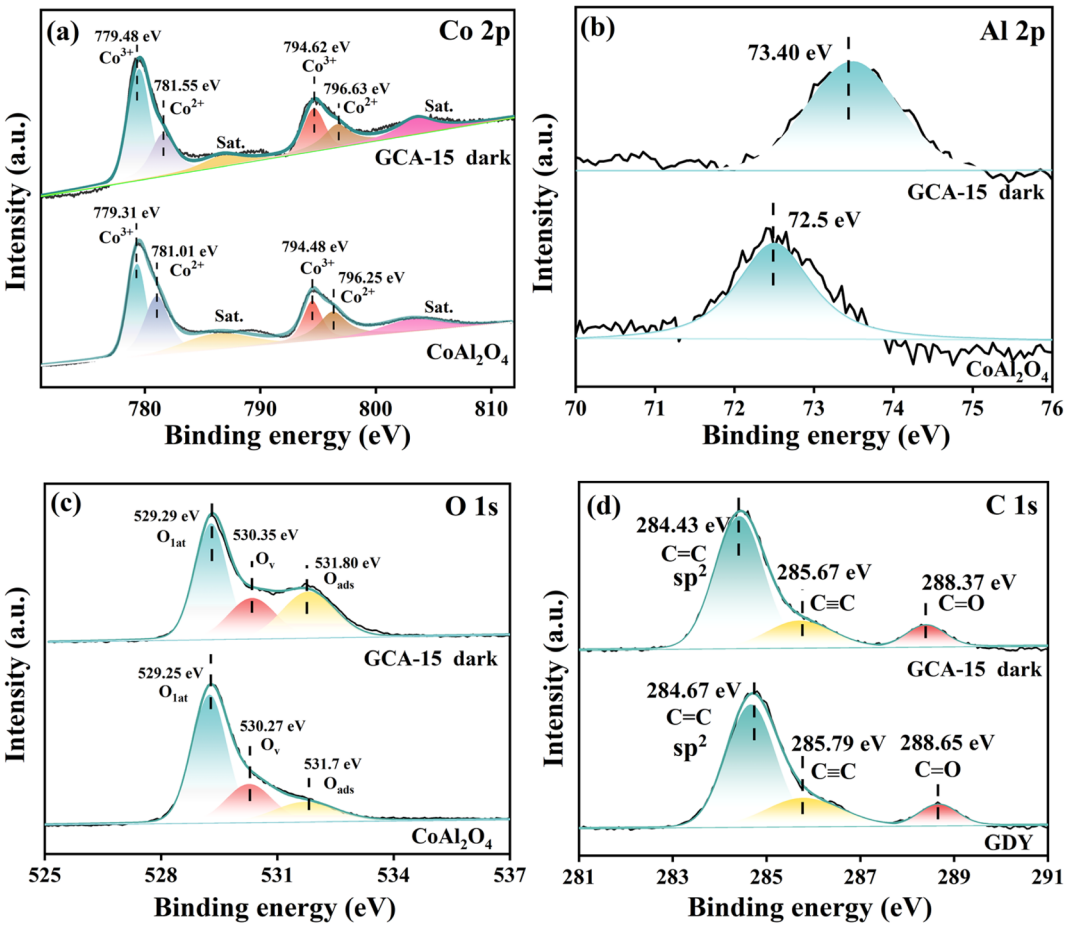

Fig. 5 (a) Co 2p XPS spectra of $CoAl_2O_4$ and GCA-15; (b) Al 2p; (c) O 1s and (d) C 1s XPS spectra of GDY and GCA-15.

(Fig. 5c), three distinguishable peaks at 529.25 eV, 530.27 eV, and 531.7 eV can be discerned. These peaks are attributed to lattice oxygen (O_{lat}), vacant oxygen (O_v), and adsorbed oxygen (O_{ads}).[29,30] The adsorbed oxygen (O_{ads}) in CoAl-LDHs primarily originates from the adsorption of oxygen on the metal hydroxide surface. The O_{ads} believed to be generated from surface bound water or adsorbed oxygen.[31] In addition, the C 1s peak of GDY is located at 284.06 eV and 285.24 eV, corresponding to C=C (sp^2) and C≡C (sp), respectively.[24] As observed in Fig. 5a–d, the binding energies of Co 2p, Al 2p and O 1s in the GCA-15 composite shift to higher energy levels in the absence of light compared to $CoAl_2O_4$. In contrast, the binding energy of C 1s in GCA-15 composites consistently shifts to lower energy levels compared to GDY, suggesting electron migration from $CoAl_2O_4$ to GDY.

The specific surface area, pore size distribution, and pore volume of GDY, CoAl-LDH, $CoAl_2O_4$ and GCA-15 were determined through N_2 adsorption and desorption experiments. The adsorption–desorption isotherms, along with relevant data, are presented in Fig. 6 and Table 1. It is evident from the figure that all samples exhibit type IV isotherms accompanied by typical type H3 hysteresis curves, indicating the presence of irregularly shaped mesoporous pores across the samples. The specific surface areas of GDY, CoAl-LDH, $CoAl_2O_4$ and GCA-15 are measured at 12.62 $m^2\ g^{-1}$, 21.51 $m^2\ g^{-1}$, 24.84 $m^2\ g^{-1}$ and 26.94 $m^2\ g^{-1}$, respectively. The difference in specific surface area between GDY and CoAl-LDH is due to their own material properties and the small specific surface area of smaller particles.[20,32] The BET surface area of $CoAl_2O_4$ is higher than that of CoAl-LDH, which is due to the high temperature annealing that creates pores on the two-dimensional nanosheets. Moreover, the BET surface area and pore size of GCA-15 exceed those of single GDY and $CoAl_2O_4$. The larger surface area and pore size of the GCA-15 heterojunction provide abundant surface active sites for photocatalytic reactions, thereby enhancing both the adsorption capacity and visible light absorption across the entire system.[33] Consequently, the elevated specific surface area of the GCA-15 catalyst serves to bolster the performance of photocatalytic H_2 reduction.

2.2 Photocatalytic activity and stability

Photocatalytic hydrogen evolution experiments were performed using TEOA aqueous solution (15 v/v%, pH = 9) as the sacrificial reagent and eosin Y (EY) as the photosensitizer under visible light irradiation.[34] As can be seen in Fig. 7a, pure GDY and $CoAl_2O_4$ show very low activities of 2.03 μmol and 31.73 μmol, respectively, and the photocatalytic activity is significantly increased after GDY coupling with $CoAl_2O_4$. As shown in Fig. 7b,

 This journal is © The Royal Society of Chemistry 2024

Published on 26 2024. Downloaded on 31.01.2026 3:43:36.

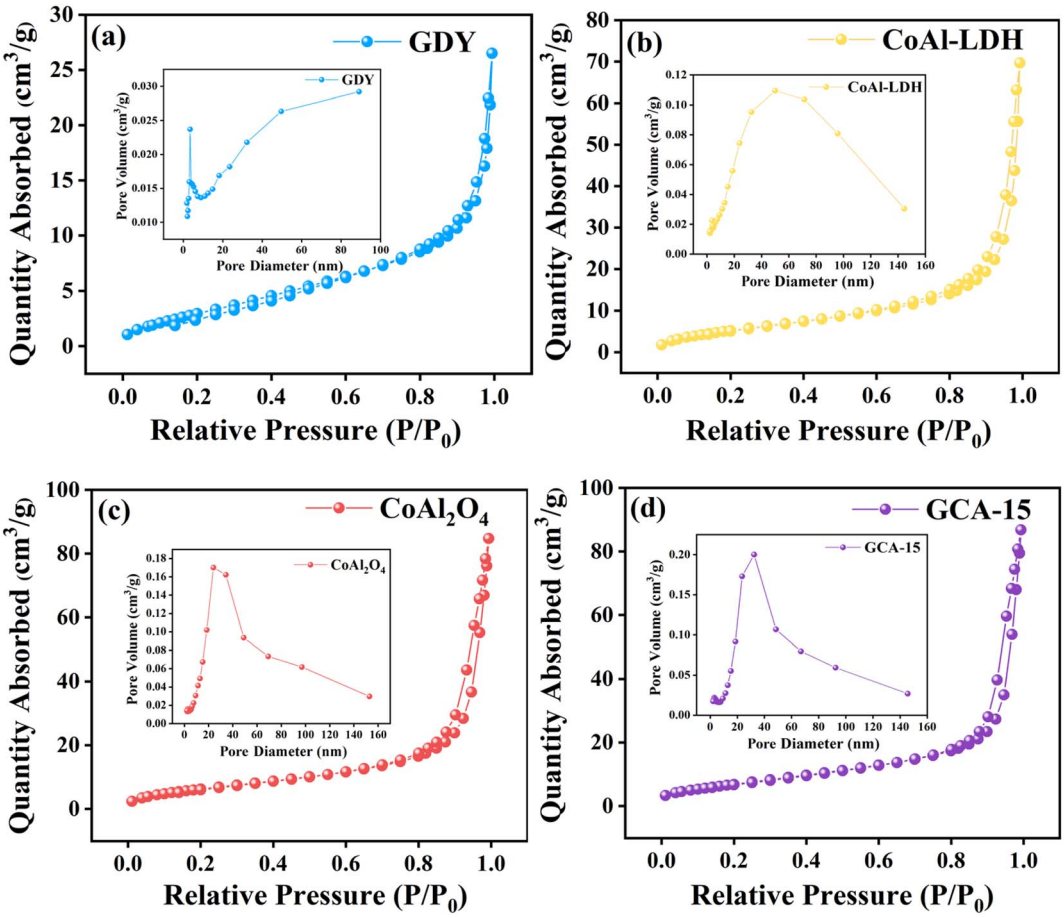

Fig. 6 N_2 adsorption–desorption isotherms of (a) GDY, (b) CoAl-LDH, (c) $CoAl_2O_4$ and (d) GCA-15 samples (inset images are the corresponding pore size distribution curves).

with the increase of GDY loading, the hydrogen production of all the GDY/$CoAl_2O_4$ composites showed a remarkable increase over 5 h. A maximum hydrogen production of 5009.28 μmol g^{-1} h^{-1} was obtained over GCA-15, which was 4.78 times higher than that of $CoAl_2O_4$. However, the hydrogen production activity gradually decreased with the loading of excess GDY, which may be due to the excess GDY leading to the intensification of agglomeration and the reduction of the active area for hydrogen production.[13,18] The doubling of hydrogen production by GCA-*X* verifies that GDY and $CoAl_2O_4$ do not carry out the photocatalytic hydrogen production reaction independently. Instead, there exists a mutually advantageous positive interaction, enhancing the catalyst hydrogen evolution capability.[35] The amorphous GDY exhibited numerous unsaturated bonds and abundant defects, which resulted in a disordered structure that increased the presence of active sites, thereby promoting surface reaction kinetics. Due to the advantages of the combined crystalline/amorphous, 2D/3D, and hierarchical architecture of GDY/$CoAl_2O_4$, the recombination of electron–hole pairs was significantly reduced, and the aggregation of GDY nanosheets was also prevented.[36] In addition, the nanosheet petals of porous $CoAl_2O_4$ provided a larger surface area to the reaction system, which promoted carrier transfer and further improved the photocatalytic hydrogen production performance of GCA.[15,16,37] Fig. S5† illustrates the comparison of hydrogen evolution activity between floral and non-floral

Table 1 S_{BET}, pore diameter, and pore volume of GDY, CoAl-LDH, $CoAl_2O_4$ and GCA-15

Samples	S_{BET} (m^2 g^{-1})	Pore volume (cm^3 g^{-1})[a]	Average pore size (nm)[a]
GDY	12.62	0.03	9.21
CoAl-LDH	21.51	0.11	18.24
$CoAl_2O_4$	24.84	0.13	19.34
GCA-15	26.94	0.14	18.05

[a] Total pore volume taken from the N_2 adsorption volume at a relative pressure (P/P_0) of 0.99.

Published on 26 2024. Downloaded on 31.01.2026 3:43:36.

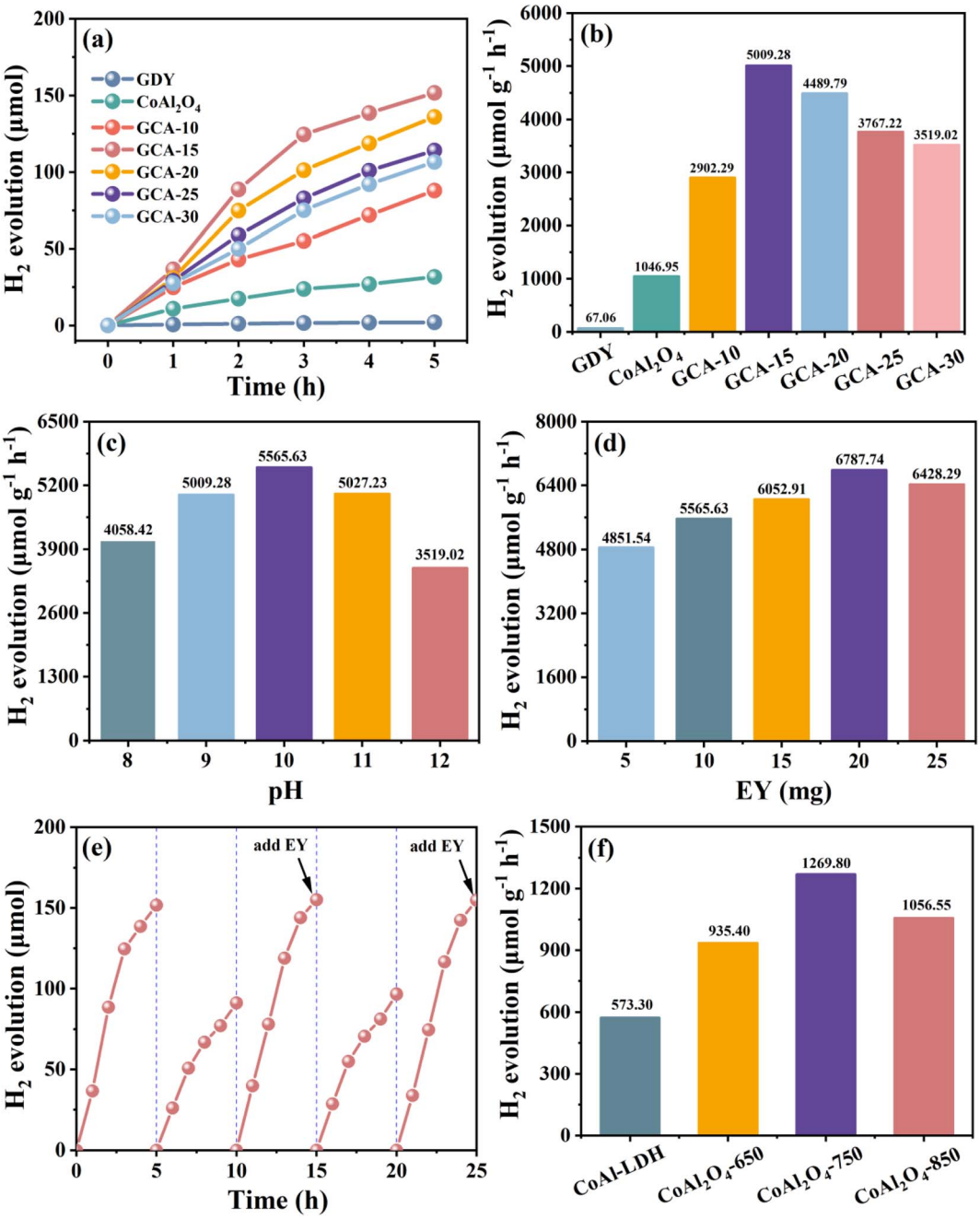

Fig. 7 (a) Photocatalytic hydrogen evolution activities of GDY, $CoAl_2O_4$ and GCA-*X* under visible light irradiation; (b) H_2 evolution rates of GDY, $CoAl_2O_4$ and GCA-*X*; photocatalytic H_2 evolution at different (c) pH and (d) EY values for GCA-15; (e) photostability of the GCA-15 photocatalyst; (f) H_2 evolution of CoAl-LDHs, $CoAl_2O_4$-650, $CoAl_2O_4$-750 and $CoAl_2O_4$-850.

$CoAl_2O_4$ structures. It can be observed that the floral structure of $CoAl_2O_4$ exhibits higher hydrogen evolution activity, which further underscores the positive influence of the 3D hierarchical structure on photocatalytic activity. Additionally, the mapping results of the non-floral $CoAl_2O_4$ are provided in Fig. S6.† Table S1† provides a comparative analysis of GDY-based composites for photocatalytic H_2 evolution activity. This comparison serves to underscore the superior performance of GDY/$CoAl_2O_4$ in photocatalysis.

At various pH values in the sacrificial reagent environment (Fig. 7c), a notable enhanced hydrogen evolution ability is observed for GCA-15, particularly at pH 9–11. The highest hydrogen evolution activity was achieved at pH = 10 and diminished when it exceeded this. This result can be attributed to the lower content of free protons in the higher pH system, which is unfavorable for the reaction. Meanwhile, the protonation of TEOA at lower pH levels results in a reduction of its electron donor capacity.[38] Fig. 7d depicts the hydrogen production outcomes of GCA-15 using different EY quantities. As the EY content in the

 This journal is © The Royal Society of Chemistry 2024

Published on 26 2024. Downloaded on 31.01.2026 3:43:36.

solution increases, the hydrogen evolution activity initially increases and subsequently decreases. The highest H_2 production rate of 6787.74 μmol g^{-1} h^{-1} is attained when 20 mg of EY is introduced. This result suggests that the photocatalytic activity may be influenced by its polymerization state, and the participation of excited electrons in photocatalytic hydrogen evolution varies with distinct EY concentrations.[39,40] At lower EY content, there are insufficient free dye molecules in the solution to effectively partake in electron transfer and adhere to the active interface. Conversely, an excessive dye concentration can result in self-quenching of the excited dye molecules, leading to a reduction in incident photons and consequently decreasing the hydrogen evolution activity.[41] Fig. 7e presents the results of cyclic hydrogen evolution experiments for GCA-15, aiming to observe its stability.

The experiments started from the second cycle, with each cycle involving the addition of 10 mg of EY. The results reveal that hydrogen production remains stable for 5 hours during cycles 1, 3, and 5, while it significantly decreases during cycles 2 and 4. This decline is primarily attributed to the degradation of EY under visible light irradiation. Additionally, continuous TEOA depletion and protonation of certain active centers may also serve as influencing factors.[42] Moreover, the stability of the composite photocatalyst was confirmed by the minimal changes observed in the XRD pattern (Fig. S7†) of GCA-15 before and after the photocatalytic reaction.

Zeta potential is a measure of the strength of mutual repulsion or attraction between particles. The zeta potential diagrams for GDY, $CoAl_2O_4$ and GCA-15 samples are presented in Fig. S8,† with values of −7.18 mV, −18.65 mV and −51.23 mV, respectively. The zeta potential of GCA-15 samples is notably more negatively charged compared to GDY and $CoAl_2O_4$. This difference can be attributed to the sonication process during GCA-15 preparation, which resulted in the exfoliation of GDY and $CoAl_2O_4$ nanosheets. This exfoliation increased the number of active sites on the surface of GCA-15, thereby enhancing its photocatalytic activity. Simultaneously, the increased electronegativity of the GCA-15 surface enhances its ability to adsorb protons (H^+), leading to a tighter binding between protons and the surface, which contributes to the photocatalytic hydrogen production reaction.[43]

Additionally, the impact of various calcination temperatures on the hydrogen production activity of CoAl-LDHs. As shown in Fig. 7f, the photocatalytic hydrogen production activity of $CoAl_2O_4$ at 750 °C (1269.80 μmol g^{-1} h^{-1}) was higher than that of 650 °C (935.40 μmol g^{-1} h^{-1}) and 850 °C (1056.55 μmol g^{-1} h^{-1}). The outstanding performance of $CoAl_2O_4$ at 750 °C can be attributed to several factors. During the calcination process, the catalyst porous structure enhances light absorption and enables multiple light reflections. Meanwhile, its large surface area provides an abundance of active sites for the reaction system.[20] Lastly, the ultra-thin nanosheets expedite the migration of charge carriers, effectively preventing the recombination of photogenerated charge carriers.[20]

2.3 Optical properties and electronic structures

The ability of a material to absorb light has an important influence on its photocatalytic performance. Therefore, the optical properties of GDY, $CoAl_2O_4$ and GCA-*X* were explored by UV-Vis diffuse reflection spectroscopy (UV-Vis DRS). As shown in Fig. 8a, the spectral curves of all the catalysts show an extremely strong light trapping ability in the range of 300–700 nm, which is related to their black color properties. Furthermore, the energy bands of GDY and $CoAl_2O_4$ are obtained by extrapolating the $(ahv)^2$–hv curve to the *x*-axis using the Tauc diagram and Kubelka–Munk technique.[24,25] As shown in Fig. 8b and c, the extrapolated band energies for GDY and $CoAl_2O_4$ are 1.79 eV and 1.69 eV, respectively. In addition, the type of GDY and $CoAl_2O_4$ semiconductor is determined from the Mott–Schottky curves, and its energy band structure is further calculated to better analyze the carrier dynamics of GCA-*X*. Fig. 8d and e illustrate the Mott–Schottky curves of GDY and $CoAl_2O_4$ at 500 Hz, where both GDY and $CoAl_2O_4$ show negative slopes, indicating that both GDY and $CoAl_2O_4$ are n-type semiconductors.[44] The flat band potentials (E_{fb}) of GDY and $CoAl_2O_4$ are −0.78 V and −1.38 V, respectively. In n-type semiconductors, the conduction band potential (E_{CB}) is generally 0.1–0.2 V more negative than the flat band potential.[45,46] Utilizing the formula $E_{NHE} = E_{CB} + 0.241$ V, the specific E_{CB} positions for GDY and $CoAl_2O_4$ were −0.64 V and −1.24 V *versus* the normal hydrogen electrode (NHE). Consequently, it can be inferred that the valence band potentials (E_{VB}) for GDY and $CoAl_2O_4$ were 1.15 V and 0.45 V *versus* NHE, as determined using the formula: $E_{VB} = E_g + E_{CB}$.[47] Finally, the detailed band structures for GDY and $CoAl_2O_4$ are illustrated in Fig. 8f.

2.4 Charge separation and electron transfer

In situ irradiated XPS was performed to examine the direction of charge carrier transfer within the GCA-15 heterojunction, confirming the existence of an S-scheme heterojunction.[48] Earlier, alterations in elemental binding energies were discussed in non-*in situ* XPS, indicating a direct association with electron density. Therefore, the alterations in binding energy of GCA-15 were examined through *in situ* irradiated XPS, and the results are illustrated in Fig. 9. The binding energies of Co 2p, Al 2p, and O 1s in GCA-15 under light irradiation experienced a noticeable shift to lower energy levels compared to $CoAl_2O_4$ in the absence of light (Fig. 9a–c). Conversely, in the C 1s spectrum, $CoAl_2O_4$ shifted towards higher energy levels under illumination. The results presented above indicated that $CoAl_2O_4$ exhibits an elevated electron charge density under light irradiation, which implies that photogenerated electrons were transferred from GDY to crystalline $CoAl_2O_4$, resulting in a reduced binding energy. Therefore, the aforementioned results offer evidence of the formation of an S-scheme heterojunction between GDY and $CoAl_2O_4$.[49]

Ultraviolet photoelectron spectroscopy (UPS) is capable of capturing information about interactions among valence electrons in the vicinity of the atomic Fermi energy level. As a result, it allows for the determination of the electron transfer pathway between GDY and $CoAl_2O_4$.[50] As illustrated in Fig. 10a and b, the work functions of GDY and $CoAl_2O_4$ are determined using the formula $\Phi = h\nu - (E_{Fermi} - E_{Cutoff})$, where $h\nu$ represents the photon energy, E_{Fermi} is the high kinetic energy starting edge,

Published on 26 2024. Downloaded on 31.01.2026 3:43:36.

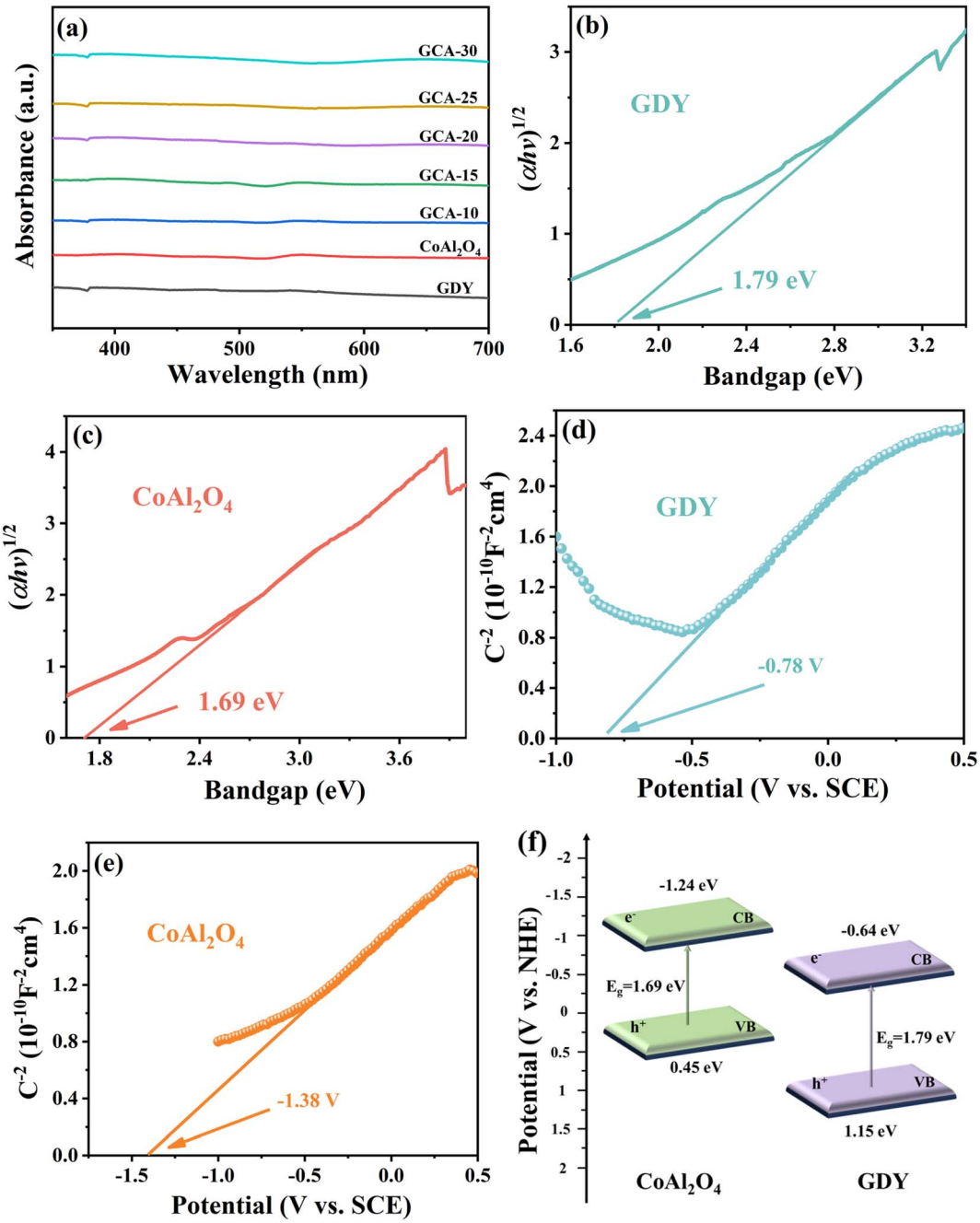

Fig. 8 (a) UV-vis diffuse reflection spectroscopy spectra of GDY, $CoAl_2O_4$ and GCA-*X*; the $(\alpha h\nu)^2$ *vs.* photo energy curves of (b) GDY and (c) $CoAl_2O_4$; Mott–Schottky plots of (d) GDY and (e) $CoAl_2O_4$; (f) band structures of the GDY and $CoAl_2O_4$ samples.

and E_{Cutoff} is the low kinetic energy cutoff edge (with $h\nu = 21.22$ eV), whose values are calculated to be 6.59 eV for GDY and 4.40 eV for $CoAl_2O_4$, respectively.[51,52] Thus, the above data suggest that GDY has a lower Fermi level compared to $CoAl_2O_4$ and infer a charge transfer route at the GCA-*X* interface. When GDY comes into contact with $CoAl_2O_4$, free electrons naturally migrate from $CoAl_2O_4$, characterized by a higher Fermi energy level, to GDY, which has a lower Fermi energy level, which results in the establishment of an internal electric field from $CoAl_2O_4$ to GDY.[15]

The peak intensity of steady-state photoluminescence spectra can indicate the energy of electron–hole pair recombination after photoexcitation. Therefore, the efficiency of GDY, $CoAl_2O_4$ and GCA-*X* photogenerated carrier separation was tested using steady-state photoluminescence (PL) spectroscopy under 480 nm excitation.[53] As shown in Fig. 11a, the pure EY solution exhibited the highest fluorescence intensity at 540 nm. The gradual decrease in fluorescence intensity upon addition of catalyst is attributed to the interaction between the catalyst and EY molecules. However, pristine GDY and $CoAl_2O_4$ still retain

 This journal is © The Royal Society of Chemistry 2024

Published on 26 2024. Downloaded on 31.01.2026 3:43:36.

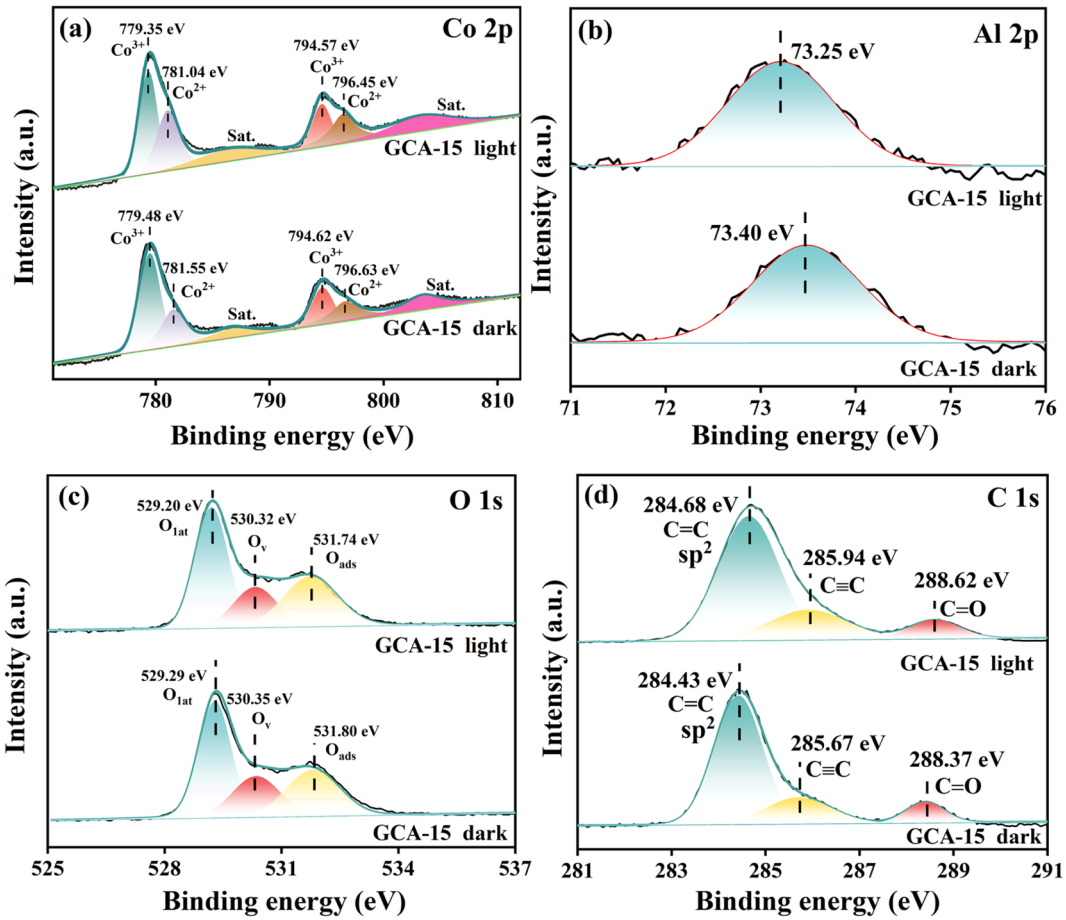

Fig. 9 *In situ* irradiated XPS spectra of (a) Co 2p (b) Al 2p (c) O 1s and (d) C 1s of GCA-15.

high PL emission intensity, which is mainly attributed to the strong recombination of photoelectrons and holes. The photoluminescence intensity of GCA-15 reaches the lowest among all catalysts, which implies that the photo-induced electron–hole pair recombination is suppressed, and the establishment of the GDY/$CoAl_2O_4$ S-scheme heterojunction is advantageous for the improvement of charge separation efficiency. Furthermore, time-resolved photoluminescence (TRPL) spectra unveiled that the GCA-15 composite had a significantly shorter average electronic lifetime of 0.32 ns compared to GDY (1.04 ns) and $CoAl_2O_4$ (1.01 ns) (Fig. 11b and Table 2). These shorter lifetimes indicate effective charge separation and improved electron transmission efficiency.[54–56]

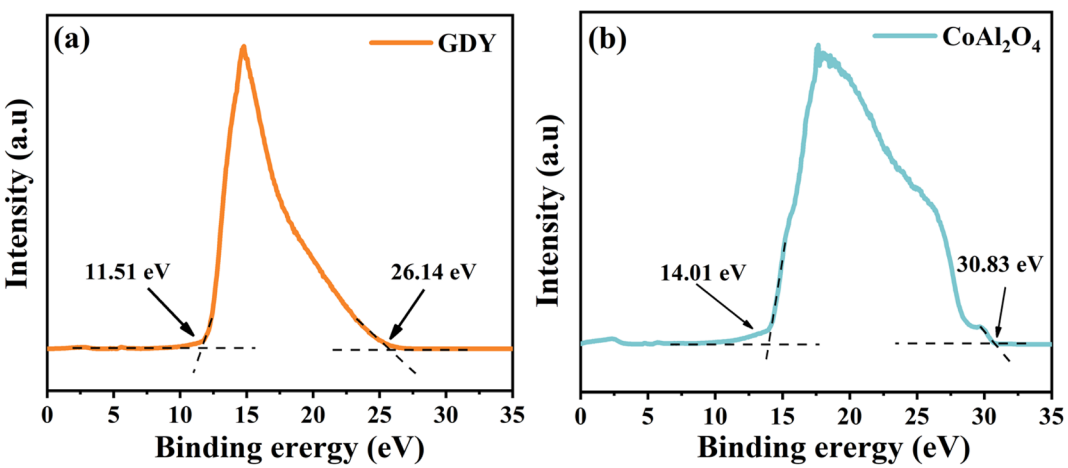

Fig. 10 UPS spectra of (a) GDY and (b) $CoAl_2O_4$.

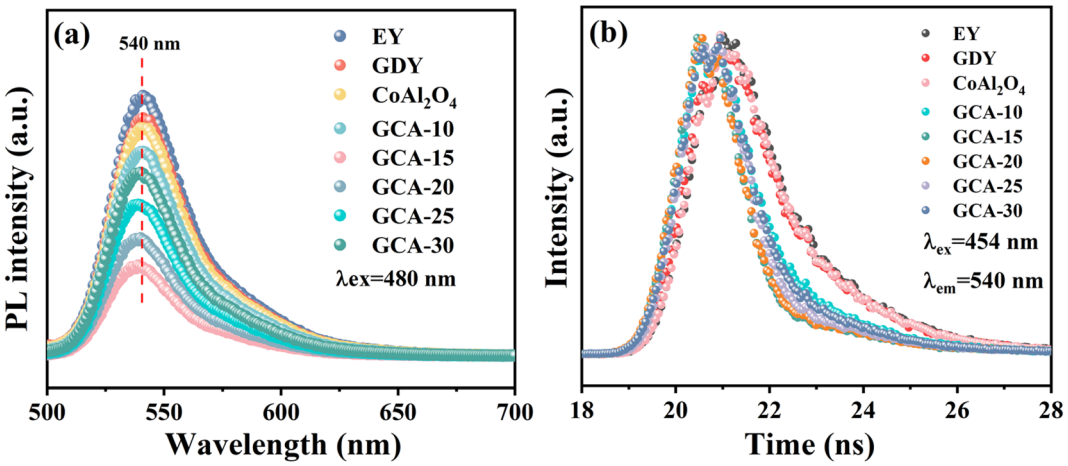

Fig. 11 PL spectra of (a) EY, GDY, $CoAl_2O_4$ and GCA-*X*; TRPL of (b) EY, GDY, $CoAl_2O_4$ and GCA-*X*.

Published on 26 2024. Downloaded on 31.01.2026 3:43:36.

It is widely acknowledged that the separation, migration and recombination of photoexcited electrons and holes are pivotal factors in photocatalytic reactions, exerting significant influence on the analysis of the system mechanisms.[57] To further explore the photovoltaic characteristics of these composites, transient photocurrent-time spectroscopy and electrochemical impedance spectroscopy (EIS) were employed to characterize and analyze GDY, $CoAl_2O_4$, and GCA-*X* nanocomposites. The quick recombination of photogenerated carriers in GDY and $CoAl_2O_4$ results in lower photocurrent intensity. Conversely, the photocurrent response increases significantly with GDY incorporation, and the composite photocatalyst demonstrates exceptional photocurrent density when the $CoAl_2O_4$ addition is at 15% (Fig. 12a). This indicates that the heterojunction interface formed by GDY and $CoAl_2O_4$ improves the transport, migration, and separation of photogenerated charges.[58] The charge transfer resistance of electrode materials was investigated through electrochemical impedance spectroscopy (EIS). All samples exhibit semicircles in the high frequency region, which corresponds to the charge transfer process. Generally, a smaller Nyquist arc radius in electrochemical impedance signifies reduced electron resistance for transport and migration, resulting in a notably higher photocarrier migration rate (Fig. 12b).[59] The inset of Fig. 12b displays an equivalent circuit fitted to the Nyquist plot, comprising a bulk solution (R1), a charge transfer resistor (R2), and a double layer capacitance (CPE1).[6] When compared to the individual GDY and $CoAl_2O_4$ phases, the GCA-15 composite photocatalyst displayed significantly reduced impedance and enhanced conductivity. This reduction signifies a decrease in interfacial charge transfer resistance, leading to improved electron transfer and favoring photocatalytic reactions.[15]

Evaluation of electrochemical activities of GDY, $CoAl_2O_4$, and GCA-*X* at applied potential is performed by linear scanning voltammetry (LSV). In Fig. 12c, GCA-15 shows a higher cathode current compared to GDY and $CoAl_2O_4$ at the same current density. This indicates an acceleration in the separation and transfer rate of photogenerated carriers, promoting

Table 2 TRPL decay parameters for EY, GDY, $CoAl_2O_4$ and GCA-*X*

Samples	Lifetime $\langle\tau\rangle$ (ns)	Pre-exponential factors *B*%	Average lifetime $\langle\tau_{av}\rangle^a$ (ns)
EY	$\tau = 1.15$	$B = 100$	1.15
GDY	$\tau_1 = 0.28$	$B_1 = 55.45$	1.04
	$\tau_2 = 1.52$	$B_2 = 44.55$	
$CoAl_2O_4$	$\tau_1 = 0.80$	$B_1 = 54.46$	1.01
	$\tau_2 = 1.49$	$B_2 = 45.54$	
GCA-10	$\tau_1 = 0.62$	$B_1 = 91.43$	0.67
	$\tau_2 = 3.02$	$B_2 = 8.57$	
GCA-15	$\tau_1 = 0.30$	$B_1 = 92.52$	0.32
	$\tau_2 = 5.13$	$B_2 = 7.48$	
GCA-20	$\tau_1 = 0.35$	$B_1 = 92.09$	0.38
	$\tau_2 = 5.28$	$B_2 = 7.91$	
GCA-25	$\tau_1 = 0.40$	$B_1 = 93.14$	0.43
	$\tau_2 = 4.70$	$B_2 = 6.86$	
GCA-30	$\tau_1 = 4.65$	$B_1 = 5.83$	0.62
	$\tau_2 = 5.83$	$B_2 = 94.17$	

 This journal is © The Royal Society of Chemistry 2024

Published on 26 2024. Downloaded on 31.01.2026 3:43:36.

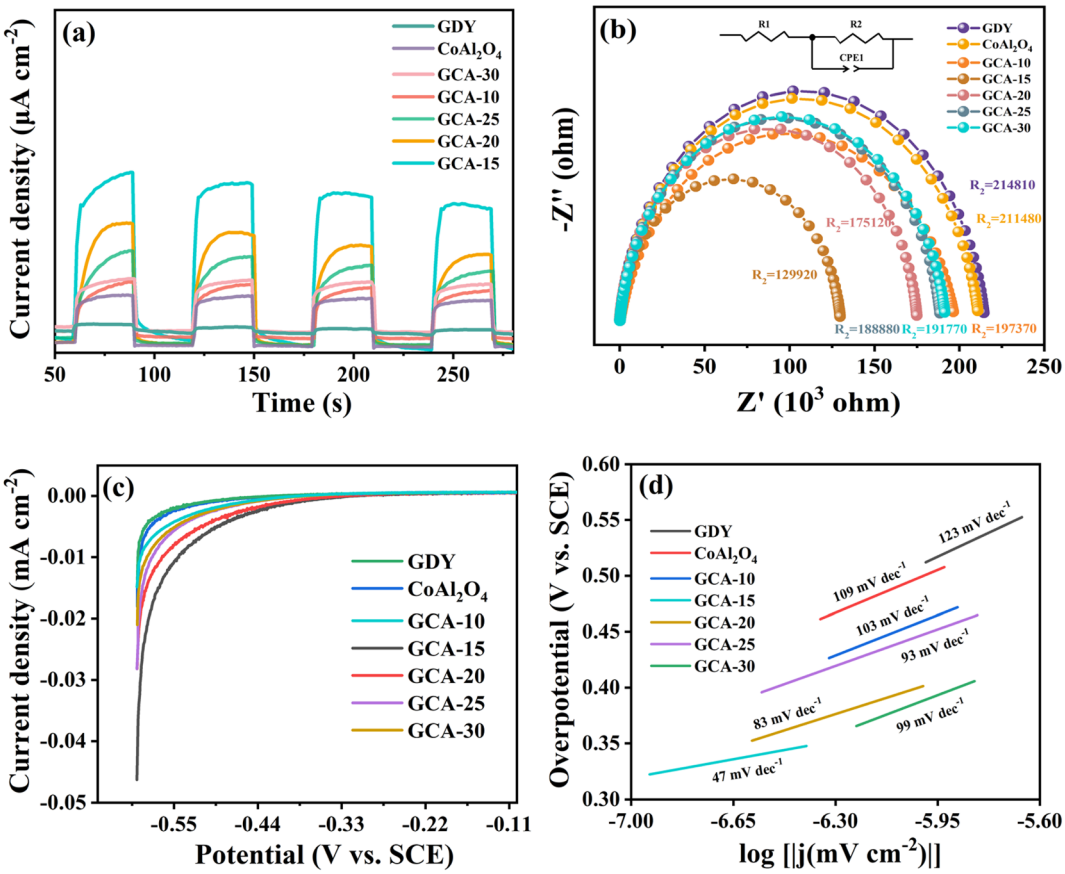

Fig. 12 (a) Transient photocurrent responses for GDY, $CoAl_2O_4$ and GCA-*X*; (b) EIS of GDY, $CoAl_2O_4$ and GCA-*X*; (c) LSV curves of GDY, $CoAl_2O_4$ and GCA-*X* and (d) the corresponding Tafel plots for GDY, $CoAl_2O_4$ and GCA-*X*.

photocatalytic hydrogen production.[60] Tafel slopes provide important information about the kinetics of photocatalytic reactions and electron transfer processes. By analyzing them, a deeper understanding of the properties of GDY, $CoAl_2O_4$ and GCA-*X* can be obtained. As demonstrated in Fig. 12d. The Tafel slopes for GDY, $CoAl_2O_4$ and GCA-15 are 123 mV dec^{-1}, 109 mV dec^{-1} and 47 mV dec^{-1}, respectively. This calculation is based on the formula ($\eta = a + b\log|j|$), where η represents the overpotential, b is the Tafel slope, and j denotes the current density.[22] The Tafel slope of GCA-15 indicates a more rapid increase in the hydrogen evolution rate in the water splitting reaction, further underscoring the exceptional hydrogen production performance of the GCA-15 catalyst.[25]

2.5 Density functional theory (DFT) calculations

The electronic structures of GDY and $CoAl_2O_4$, including the energy band structure as well as the density of electronic states, have been investigated using DFT calculations (using the generalized gradient approximation-Perdew–Burke–Ernzerhof), thus revealing the electron transport properties of the material. As seen in Fig. 13a and d, DFT optimization models were established for GDY and $CoAl_2O_4$.[61,62] The simulated energy band structures yielded theoretical bandgap E_g values of 0.577 eV for GDY and 1.690 eV for $CoAl_2O_4$ monolithic materials. Notably, the $CoAl_2O_4$ value closely approximated the experimental value. It's important to mention that the calculated bandgap of GDY (0.577 eV) is significantly lower than the measured value (1.79 eV). This underestimation is a common characteristic of the PBE functional, which tends to underestimate the bandgap but doesn't affect the accuracy of other calculated properties.[63] Of secondary importance, the edge electron pathways of the GDY conduction band (CB) and valence band (VB) exhibit symmetry, suggesting that GDY possesses characteristics of a second-order, two-dimensional topological insulator.[64] Fig. 13c illustrates that GDY is a typical semiconductor. The VB top of GDY contains electrons mainly in the C 2p and C 1s states, with a predominance of electrons in the C 2p state.[41] The density of states for $CoAl_2O_4$ surfaces in several spin orbitals and the states near the Fermi energy level come predominantly from the Co, Al, and O ions. The $CoAl_2O_4$ VB and CB depend mainly on electrons from the Co 3d, Al 3d and O 2p states. Among them, Al 3d and Co 3d play a dominant role in the VB, while the CB is dominated by Al 3d and O 2p.[65] The above findings reveal the electronic orbital states of GDY and $CoAl_2O_4$, which can help understand the charge migration process and photocatalytic active sites.

To further ascertain the direction of electron migration within the heterojunction, we estimated the work functions of GDY and $CoAl_2O_4$ through DFT calculations.[41] The work

Published on 26 2024. Downloaded on 31.01.2026 3:43:36.

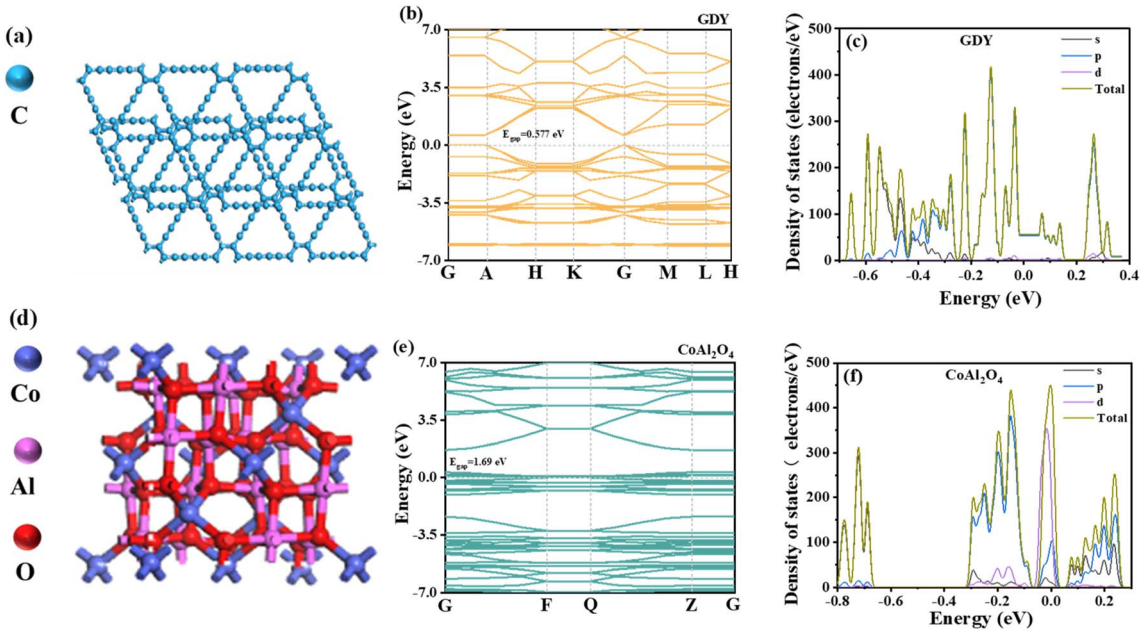

Fig. 13 (a and d) The unit cell of GDY and $CoAl_2O_4$; (b and e) band structure of GDY and $CoAl_2O_4$; (c and f) densities of states of GDY and $CoAl_2O_4$.

function is a key parameter used to characterize the electronic properties of a material and its interaction with other materials or the environment. In semiconductor photocatalytic heterojunction materials, a lower work function means that the electrons within the semiconductor are more likely to migrate to the other side.[66] As shown in Fig. 14a and b, the work functions of GDY and $CoAl_2O_4$ with respect to the vacuum energy levels are calculated to be 5.53 eV and 5.23 eV, respectively, consistent with the pattern of change in the experimental values. The work function values suggest that when a heterojunction interface is formed between the two contacts, electrons from the $CoAl_2O_4$ nanosheet will migrate through the interface to GDY until an equilibrium is established between the Fermi energy levels of both components.[67] In addition, the charge density differential can present the difference in charge distribution near the heterojunction interface for more intuitive observation of the electron transfer information within the heterojunction. In photocatalytic heterojunction materials, a positive charge density differentia indicates that the photogenerated electrons are more inclined to move in a certain direction, which contributes to the improvement of photocatalytic activity, especially in the case of separation of photogenerated electrons and holes. Therefore, by investigating the charge density differentia in heterojunctions, it is possible to gain a deeper understanding of the performance of photocatalytic materials and optimize the heterojunction design. As shown in Fig. 14c, a GCA heterojunction geometry model was established to calculate the charge differential density. Among them, the yellow region represents the accumulation of electrons and the blue color represents the depletion of electrons, and it is not difficult to see that in GCA, electrons are more inclined to transfer from the GDY layer to $CoAl_2O_4$ through the interface. This charge transfer outcome suggests a robust electron coupling between $CoAl_2O_4$ and GDY, with the electrons primarily transferring from GDY to $CoAl_2O_4$. This result aligns with the XPS results.

2.6 Possible photocatalytic hydrogen evolution mechanism

Hence, considering the analysis of the results presented above, we propose a plausible S-scheme mechanism for the GDY/$CoAl_2O_4$ heterojunction (Fig. 15). The Fermi level of $CoAl_2O_4$ is relatively high, while that of GDY is relatively low. Thermodynamically, when GDY forms a close interface with $CoAl_2O_4$, electrons in $CoAl_2O_4$ spontaneously migrate to GDY at the interface until equilibrium in E_f is achieved. In this context, $CoAl_2O_4$ carries positive charges, whereas GDY exhibits negative charges. As a result, an IEF is established with the direction from $CoAl_2O_4$ to GDY. Under sunlight irradiation, electrons in the valence band (VB) of GDY and $CoAl_2O_4$ become excited, moving into their respective conduction bands (CBs) and leaving holes in their respective valence bands (VBs). The excited electrons in the conduction band (CB) of GDY combine with the holes in the valence band (VB) of $CoAl_2O_4$, driven by the internal electric field at the heterojunction interface. Subsequently, EY is photoexcited to a single excited state EY^{1*} and undergoes intersystem crossing to produce the more stable EY^{3*}. EY^{3*} is reduced and quenched by TEOA to form $EY^{-\bullet}$. The electrons from EY are transferred to the CB of GCA-15 to participate in the photocatalytic production of H_2, while the EY molecule returns to the ground state.[41] The holes in the valence band (VB) of GDY are involved in the oxidation of TEOA, while the photogenerated electrons accumulated on $CoAl_2O_4$ actively participate in the water splitting reaction. Based on the above analysis, we proposed a possible photocatalytic hydrogen production mechanism for GCA-*X*.

 This journal is © The Royal Society of Chemistry 2024

Published on 26 2024. Downloaded on 31.01.2026 3:43:36.

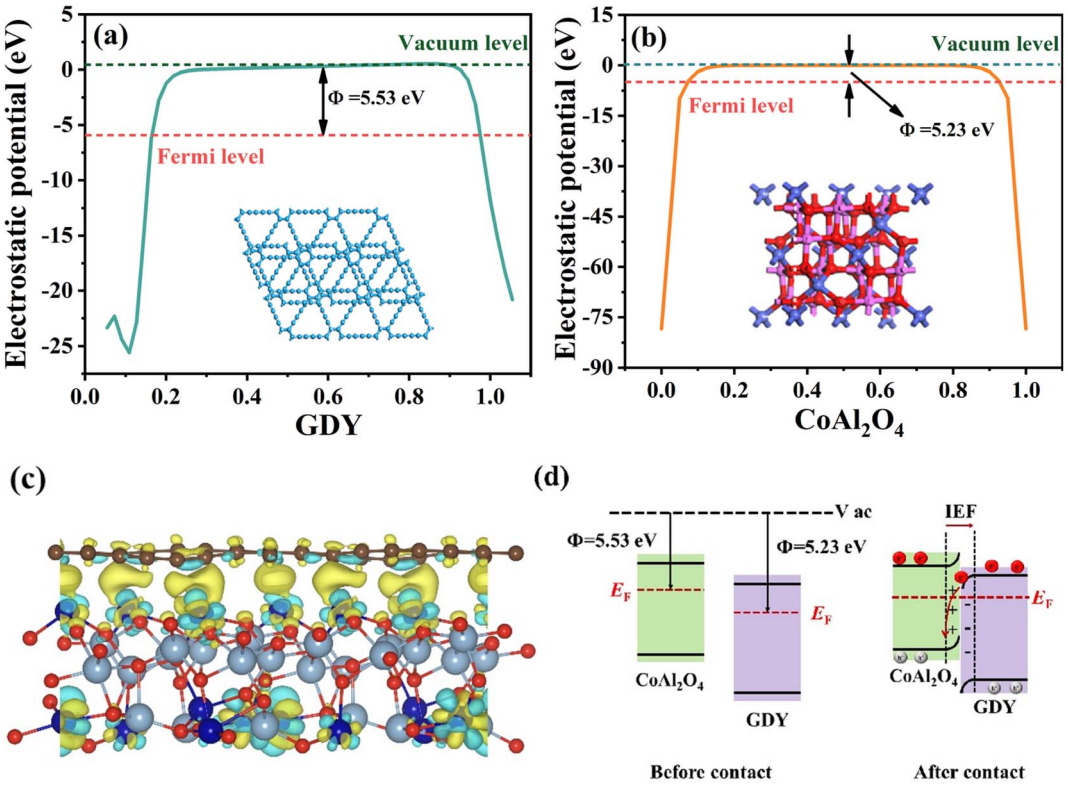

Fig. 14 The calculated work functions of (a) GDY and (b) $CoAl_2O_4$; (c) the charge density difference of GDY/$CoAl_2O_4$; the blue and yellow regions represent the consumption and accumulation of electrons. (d) The charge transfer route at the interface of GCA-*X*.

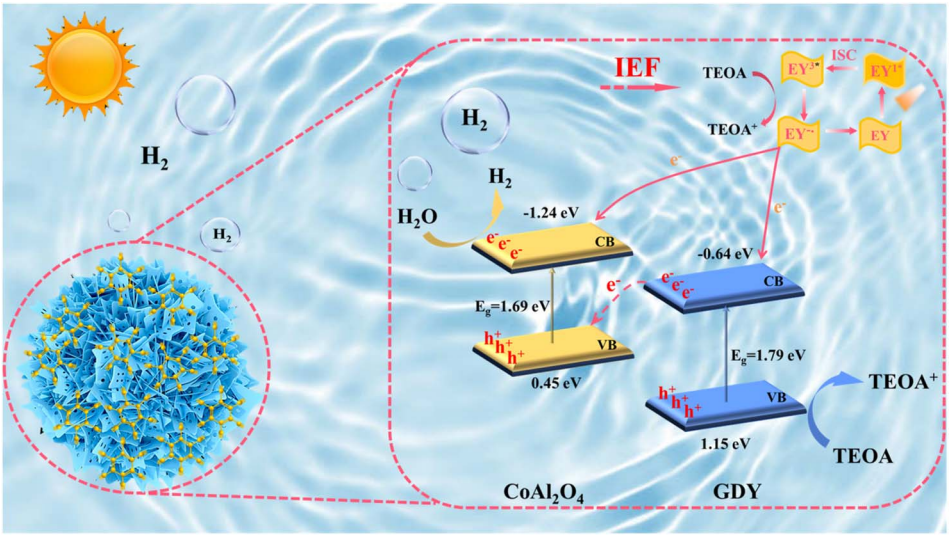

Fig. 15 The charge transfer mechanism over the GDY/$CoAl_2O_4$ S-scheme heterojunction.

3. Conclusion

In conclusion, a hierarchical S-scheme 2D/3D GDY/$CoAl_2O_4$ heterojunction was synthesized using porous $CoAl_2O_4$ nanoflowers loaded with GDY nanosheets. The 3D porous $CoAl_2O_4$ nanoflowers possess ultrathin nanosheets by calcination transformation of CoAl-LDHs. The porous structure provides a large amount of reactive surface area and abundant adsorption sites for the hydrogen production reaction, thus increasing the efficiency of the photocatalytic reaction. The hierarchical architecture of $CoAl_2O_4$ nanoflowers with ultrathin nanosheets can effectively enhance the charge separation and electron transfer. More significantly, the exceptional photostable and highest photocatalytic hydrogen evolution activity of 5009.28

Published on 26 2024. Downloaded on 31.01.2026 3:43:36.

μmol g^{-1} h^{-1} were obtained over GCA-15, which is a 4.78-fold increase compared to $CoAl_2O_4$ alone. The excellent photocatalytic activity can be attributed to the coupling of GDY with 3D porous $CoAl_2O_4$ leading to the rearrangement of the energy band structure and the formation of tightly bonded S-scheme heterojunctions, which promote the separation of photogenerated carriers and interfacial electron transfer. In addition, the hierarchical structure not only retains the properties of the original lamellar unit structure, but the coupling effect with GDY also confers a higher charge transport capability to the hierarchical heterojunction material. Most importantly, the S-scheme mechanism was verified by the UPS, DFT and *in situ* irradiated XPS results. The charge density difference is even more intuitive to confirm that the electrons are transferred from GDY to $CoAl_2O_4$ in GCA. This work provided a simple strategy for design and construction of hierarchical graphdiyne-based S-scheme heterostructures for photocatalytic hydrogen production.

Author contributions

Xuqiang Hao: conceptualization, writing-review & editing, supervision, project administration, funding acquisition. Wei Deng: methodology, investigation, validation, formal analysis, visualization, writing-original draft, data curation. Yu Fan: methodology, formal analysis. Zhiliang Jin: writing-review & editing, supervision.

Conflicts of interest

The authors declare that they have no known competing financial interests or personal relationships that could have appeared to influence the work reported in this paper.

Acknowledgements

This work was financially supported by Fundamental Research Funds for the Central Universities of North Minzu University (2021KYQD18) and the Ningxia Natural Science Foundation (2022AAC05034).

References

1 H. Li, H. Gong and Z. Jin, In_2O_3-Modified Three-Dimensional Nanoflower MoS_x Form S-scheme Heterojunction for Efficient Hydrogen Production, *Acta Phys. -Chim. Sin.*, 2022, **38**, 220103.

2 Z. Li, H. Fang, Z. Chen, W. Zou, C. Zhao and X. Yang, Regulating donor-acceptor interactions in triazine-based conjugated polymers for boosted photocatalytic hydrogen production, *Appl. Catal. B Environ.*, 2022, **312**, 121374.

3 X. Xue, W. Dong, Q. Luan, H. Gao and G. Wang, Novel interfacial lateral electron migration pathway formed by constructing metallized CoP_2/CdS interface for excellent photocatalytic hydrogen production, *Appl. Catal. B Environ.*, 2023, **334**, 122860.

4 F. Xu and B. Weng, Photocatalytic hydrogen production: an overview of new advances in structural tuning strategies, *J. Mater. Chem. A*, 2023, **11**, 4473–4486.

5 Z. Lan, X. Chi, M. Wu, X. Zhang, X. Chen, G. Zhang and X. Wang, Molecular Design of Covalent Triazine Frameworks with Anisotropic Charge Migration for Photocatalytic Hydrogen Production, *Small*, 2022, **18**, 2200129.

6 L. Zhang, J. Zhang, H. Yu and J. Yu, Emerging S-Scheme Photocatalyst, *Adv. Mater.*, 2022, **34**, 2107668.

7 L. Li, S. Fu, D. Tao, J. Zhang, M. Tian, J. Shi, M. Ma and C. He, Heterobimetallic $CoCeO_x$ derived from cobalt partially-substituted Ce-UiO-66 for chlorobenzene efficient catalytic destruction, *J. Rare Earths*, 2023, **41**, 810–819.

8 L. Li, J. Shi, M. Tian, Y. Zhao, S. Chai and C. He, Catalytic efficient destruction of chlorobenzene and 1,2-dichlorobenzene over $La_{0.9}Sr_{0.1}MnO_3$ engineered by a scalable surface reconstruction strategy, *Fuel*, 2023, **334**, 126564.

9 S. Liu, K. Wang, M. Yang and Z. Jin, Rationally Designed $Mn_{0.2}Cd_{0.8}S$@CoAl LDH S-Scheme Heterojunction for Efficient Photocatalytic Hydrogen Production, *Acta Phys. -Chim. Sin.*, 2022, **38**, 210902.

10 Z. Jiang, B. Cheng, L. Zhang, Z. Zhang and C. Bie, A review on ZnO-based S-scheme heterojunction photocatalysts, *Chin. J. Catal.*, 2023, **52**, 32–49.

11 X. Wu, G. Chen, J. Wang, J. Li and G. Wang, Review on S-Scheme Heterojunctions for Photocatalytic Hydrogen Evolution, *Acta Phys. -Chim. Sin.*, 2023, **39**, 2212016.

12 M. Gu, L. Zhang, S. Mao, Y. Zou, D. Ma, J. Shi, N. Yang, C. Fu, X. Zhao, X. Xu, Y. Cheng and J. Zhang, Violet phosphorus: an effective metal-free elemental photocatalyst for hydrogen evolution, *Chem. Commun.*, 2022, **58**, 12811–12814.

13 X. Bai, L. Guo, T. Jia, D. Hao, C. Wang, H. Li and R. Zong, Perylene diimide growth on both sides of carbon nanotubes for remarkably boosted photocatalytic degradation of diclofenac, *J. Hazard. Mater.*, 2022, **435**, 128992.

14 Y. Fang, Y. Liu, L. Qi, Y. Xue and Y. Li, 2D graphdiyne: an emerging carbon material, *Chem. Soc. Rev.*, 2022, **51**, 2681–2709.

15 W. Deng, X. Hao, Y. Shao, S. Guo and Z. Jin, Construction of 2D-2D S-scheme heterojunction based graphdiyne (g-C_nH_{2n-2}) coupling with highly crystalline nitrogen defect g-C_3N_4 for efficient photocatalytic overall water splitting, *Sep. Purif. Technol.*, 2023, **323**, 124375.

16 R. Gao, H. He, J. Bai, L. Hao, R. Shen, P. Zhang, Y. Li and X. Li, Pyrene-benzothiadiazole-based Polymer/CdS 2D/2D Organic/Inorganic Hybrid S-scheme Heterojunction for Efficient Photocatalytic H_2 Evolution, *Chin. J. Struct. Chem.*, 2022, **41**, 2206031–2206038.

17 J. Zheng and L. Zhang, Incorporation of CoO nanoparticles in 3D marigold flower-like hierarchical architecture $MnCo_2O_4$ for highly boosting solar light photo-oxidation and reduction ability, *Appl. Catal. B Environ.*, 2018, **237**, 1–8.

18 C. Li, R. Guo, Z. Zhang, T. Wu, C. Yue and W. Pan, Loading metal nanoparticles on the CoAl-LDH/CGCNN S-scheme

 This journal is © The Royal Society of Chemistry 2024

Published on 26 2024. Downloaded on 31.01.2026 3:43:36.

heterojunction for efficient photocatalytic CO_2 reduction under visible light, *Sep. Purif. Technol.*, 2023, **322**, 124266.
19 J. Tao, X. Yu, Q. Liu, G. Liu and H. Tang, Internal electric field induced S–scheme heterojunction MoS_2/CoAl LDH for enhanced photocatalytic hydrogen evolution, *J. Colloid Interface Sci.*, 2021, **585**, 470–479.
20 F. Lv, W. Zhang, L. He, X. Bai, Y. Song and Y. Zhao, 3D porous flower-like $CoAl_2O_4$ to boost the photocatalytic CO_2 reduction reaction, *J. Mater. Chem. A*, 2023, **11**, 2826–2835.
21 K. Zhang, H. Chen, W. Pei, H. Dai, J. Li and Y. Zhu, Enhanced photocatalytic performance of $Bi_4O_5Br_2$ with three-dimensionally ordered macroporous structure for phenol removal, *Nano Res.*, 2023, **16**, 8871–8881.
22 Y. Sun, Y. Li, J. He, L. Chen, H. Ji, Z. Qin and T. Su, Controlled synthesis of $Mn_xCd_{1-x}S$ for enhanced visible-light driven photocatalytic hydrogen evolution, *Chin. J. Struct. Chem.*, 2023, **42**, 100145.
23 M. Arunkumar and A. Nesaraj, Facile chemical fabrication of Ni doped $CoAl_2O_4$ nano-spinel photocatalysts: physico-chemical properties and photodegradation of toxic malachite green dye under visible light, *Int. J. Environ. Anal. Chem.*, 2023, **103**, 1086–1106.
24 Q. Xiao, T. Yang, X. Guo and Z. Jin, S-scheme heterojunction constructed by ZnCdS and $CoWO_4$ nano-ions promotes photocatalytic hydrogen production, *Surf. Interfaces*, 2023, **43**, 103577.
25 Y. Cao, H. Gou, P. Zhu and Z. Jin, Ingenious Design of CoAl-LDH p–n Heterojunction Based on Cul as Holes Receptor for Photocatalytic Hydrogen Evolution, *Chin. J. Struct. Chem.*, 2022, **41**, 2206079–2206085.
26 Y. Guo, X. Hong, Y. Wang, Q. Li, J. Meng, R. Dai, X. Liu, L. He and L. Mai, Multicomponent Hierarchical Cu-Doped NiCo-LDH/CuO Double Arrays for Ultralong-Life Hybrid Fiber Supercapacitor, *Adv. Funct. Mater.*, 2019, **29**, 1809004.
27 L. Wang, B. Cheng, L. Zhang and J. Yu, In situ Irradiated XPS Investigation on S-Scheme TiO_2@$ZnIn_2S_4$ Photocatalyst for Efficient Photocatalytic CO_2 Reduction, *Small*, 2021, **17**, 2103447.
28 A. Roniboss, A. Subramani, R. Ramamoorthy, S. Yuvaraj, M. Sundararajan and C. Dash, Investigation of structural, optical and magnetic behavior of MAl_2O_4 (M= Zn and Co) nanoparticles via microwave combustion technique, *Mater. Sci. Semicond. Process.*, 2021, **123**, 105507.
29 G. Zheng, C. Wu, J. Wang, S. Mo, Z. Zou, B. Zhou and F. Long, Space-Confined Effect One-Pot Synthesis of γ-AlO(OH)/MgAl-LDH Heterostructures with Excellent Adsorption Performance, *Nanoscale Res. Lett.*, 2019, **14**, 281.
30 L. Peng, C. Yu, Y. Ma, G. Xie, X. Xie, Z. Wu and N. Zhang, Self-assembled transition metal chalcogenides@CoAl-LDH 2D/2D heterostructures with enhanced photoactivity for hydrogen evolution, *Inorg. Chem. Front.*, 2022, **9**, 994–1005.
31 S. A Rawool, K. K Yadav and V. Polshettiwar, Defective TiO_2 for photocatalytic CO_2 conversion to fuels and chemicals, *Chem. Sci.*, 2021, **12**, 4267–4299.
32 H. Li, X. Hao, H. Gong, Z. Jin and T. Zhao, Efficient hydrogen production at a rationally designed $MoSe_2$@Co_3O_4 p–n heterojunction, *J. Colloid Interface Sci.*, 2021, **586**, 84–94.
33 H. Chai, C. Yang, P. Xu, P. Wang, J. Qu and G. Zhang, Enhanced visible-light photocatalytic activity with Fe_2O_3–ZnO@C/g-C_3N_4 heterojunction: characterization, kinetics, and mechanisms, *J. Clean. Prod.*, 2022, **377**, 134511.
34 T. Yan, X. Zhang, H. Liu and Z. Jin, CeO_2 Particles Anchored to Ni_2P Nanoplate for Efficient Photo-catalytic Hydrogen Evolution, *Chin. J. Struct. Chem.*, 2022, **41**, 2201047–2201053.
35 H. Lv, H. Yin, N. Jiao, C. Yuan, S. Weng, K. Zhou, Y. Dang, X. Wang, Z. Lu and Y. Zhang, Efficient Charge Transfer and Effective Active Sites in Lead-Free Halide Double Perovskite S-Scheme Heterojunctions for Photocatalytic H_2 Evolution, *Small Methods*, 2023, **7**, 2201365.
36 L. Zhang, Y. Wu, J. Li, Z. Jin, Y. Li and N. Tsubaki, Amorphous/crystalline heterojunction interface driving the spatial separation of charge carriers for efficient photocatalytic hydrogen evolution, *Mater. Today Phys.*, 2022, **27**, 100767.
37 Y. Shao, X. Hao, S. Lu and Z. Jin, Molten salt-assisted synthesis of nitrogen-vacancy crystalline graphitic carbon nitride with tunable band structures for efficient photocatalytic overall water splitting, *Chem. Eng. J.*, 2023, **454**, 140123.
38 Y. Fan, X. Hao, J. Wang, Z. Hu and Z. Jin, Construction of 0D/2D Ni_2P/Ni_2P homophase Schottky junction by molten salt-assisted strategy for enhanced photocatalytic H_2 evolution, *Surf. Interfaces*, 2023, **42**, 103512.
39 J. Shi, F. Chen, L. Hou, G. Li, Y. Li, X. Guan, H. Liu and L. Guo, Eosin Y bidentately bridged on UiO-66-NH_2 by solvothermal treatment towards enhanced visible-light-driven photocatalytic H_2 production, *Appl. Catal. B Environ.*, 2021, **280**, 119385.
40 L. Shi, Y. Wang, Y. Yan, F. Liu, Z. Huang, X. Ren, H. Zhang, Y. Li and J. Ye, Synergy of heterojunction and interfacial strain for boosting photocatalytic H_2 evolution of black phosphorus nanosheets, *J. Colloid Interface Sci.*, 2022, **627**, 969–977.
41 Z. Jin and Y. Wu, Novel preparation strategy of graphdiyne (C_nH_{2n-2}): one-pot conjugation and S-Scheme heterojunctions formed with MoP characterized with in situ XPS for efficiently photocatalytic hydrogen evolution, *Appl. Catal. B Environ.*, 2023, **327**, 122461.
42 L. Yang, J. Huang, L. Shi, L. Cao, W. Zhou, K. Chang, X. Meng, G. Liu, Y. Jie and J. Ye, Efficient hydrogen evolution over Sb doped SnO_2 photocatalyst sensitized by Eosin Y under visible light irradiation, *Nano Energy*, 2017, **36**, 331–340.
43 X. Yan and Z. Jin, Interface engineering: NiAl-LDH in-situ derived NiP_2 quantum dots and Cu_3P nanoparticles ingeniously constructed p–n heterojunction for photocatalytic hydrogen evolution, *Chem. Eng. J.*, 2021, **420**, 127682.
44 R. Fu, Y. Wang, G. Wang, Q. Zhan, L. Zhang and L. Liu, Defective ZrO_{2-x} supported Ru nanoparticles as a Mott–Schottky photocatalyst for efficient ammonia synthesis under ambient conditions, *Green Chem.*, 2023, **25**, 8531–8538.

Published on 26 2024. Downloaded on 31.01.2026 3:43:36.

45 X. Zhu, Z. Pan, Y. Liu, S. Kang, L. Wang and W. Lu, Composition-dependent activity of Mn-doping NiS_2 nanosheets for boosting photocatalytic H_2 evolution, *J. Colloid Interface Sci.*, 2023, **629**, 22–35.
46 Z. Si, M. Pei, Y. Liu, B. Li and F. Kang, Boosting the photocatalytic activity of β-FeOOH catalyst for toluene oxidation by constructing internal electric field at 0D/1D homojunction interfaces, *J. Colloid Interface Sci.*, 2024, **654**, 300–307.
47 C. Yang, D. Bu and S. Huang, Three-Dimensional Porous Boron Nitride with Enriched Defects and Free Radicals Enables High Photocatalytic Activity for Hydrogen Evolution, *Chem. Eng. J.*, 2022, **446**, 137026.
48 Z. Jin and X. Wang, In situ XPS proved efficient charge transfer and ion adsorption of $ZnCo_2O_4$/CoS S-Scheme heterojunctions for photocatalytic hydrogen evolution, *Mater. Today Energy*, 2022, **30**, 101164.
49 L. Zhang, Y. Wu, N. Tsubaki and Z. Jin, 2D/3D S-Scheme Heterojunction Interface of CeO_2-Cu_2O Promotes Ordered Charge Transfer for Efficient Photocatalytic Hydrogen Evolution, *Acta Phys. -Chim. Sin.*, 2023, **39**, 2302051.
50 Y. Dang, J. Tian, W. Wang and B. Ma, Insight into the whole characteristics of (Pd/WP)/CdS for photocatalytic hydrogen evolution, *J. Colloid Interface Sci.*, 2023, **633**, 649–656.
51 M. Dai, Z. He, W. Cao, J. Zhang, W. Chen, Q. Jin, W. Que and S. Wang, Rational construction of S-scheme BN/MXene/$ZnIn_2S_4$ heterojunction with interface engineering for efficient photocatalytic hydrogen production and chlorophenols degradation, *Sep. Purif. Technol.*, 2023, **309**, 123004.
52 J. Bai, R. Shen, Z. Jiang, P. Zhang, Y. Li and X. Li, Integration of 2D layered CdS/WO_3 S-scheme heterojunctions and metallic Ti_3C_2 MXene-based Ohmic junctions for effective photocatalytic H_2 generation, *Chin. J. Catal.*, 2022, **43**, 359–369.
53 P. Ju, L. Hao, Y. Zhang, J. Sun, K. Dou, Z. Lu, D. Liao and X. Zhai, Chengjun Sun, In-situ topotactic construction of novel rod-like Bi_2S_3/Bi_5O_7I p–n heterojunctions with highly enhanced photocatalytic activities, *J. Mater. Sci. Technol.*, 2023, **135**, 126–141.
54 Y. Luo, H. Han, G. Zhang, Q. Wang and Y. Jia, Construction of Z-scheme α-Fe_2O_3/graphene/Bi_2O_2S heterojunction for visible-light-driven photocatalytic CO_2 conversion, *Sep. Purif. Technol.*, 2023, **314**, 123607.
55 S. Lv, H. Liu, J. Zhang, Q. Wu and F. Wang, Water promoted photocatalytic transfer hydrogenation of furfural to furfural alcohol over ultralow loading metal supported on TiO_2, *J. Energy Chem.*, 2022, **73**, 259–267.
56 J. He, X. Wang, S. Jin, Z. Liu and M. Zhu, 2D metal-free heterostructure of covalent triazine framework/g-C_3N_4 for enhanced photocatalytic CO_2 reduction with high selectivity, *Chin. J. Catal.*, 2022, **43**, 1306–1315.
57 Y. Li, L. Yang, H. He, L. Sun, H. Wang, X. Fang, Y. Zhao, D. Zheng, Y. Qi, Z. Li and W. Deng, In situ photodeposition of platinum clusters on a covalent organic framework for photocatalytic hydrogen production, *Nat. Commun.*, 2022, **13**, 1355.
58 X. Ma and H. Cheng, Synergy of nitrogen vacancies and intercalation of carbon species for enhancing sunlight photocatalytic hydrogen production of carbon nitride, *Appl. Catal. B Environ.*, 2022, **314**, 121497.
59 L. Dai, A. Dong, X. Meng, H. Liu, Y. Li, P. Li and B. Wang, Enhancement of Visible-Light-Driven Hydrogen Evolution Activity of 2D π-Conjugated Bipyridine-Based Covalent Organic Frameworks via Post-Protonation, *Angew. Chem., Int. Ed.*, 2023, **62**, e202300224.
60 X. Ma, W. Li, H. Li, M. Dong, L. Geng, T. Wang, H. Zhou, Y. Li and M. Li, Novel noble-metal-free Co_2P/$CdIn_2S_4$ heterojunction photocatalysts for elevated photocatalytic H_2 production: light absorption, charge separation and active site, *J. Colloid Interface Sci.*, 2023, **639**, 87–95.
61 Q. Ni, X. Ke, W. Qian, Z. Yan, J. Luan and W. Liu, Insight into tetracycline photocatalytic degradation mechanism in a wide pH range on BiOI/BiOBr: coupling DFT/QSAR simulations with experiments, *Appl. Catal. B Environ.*, 2024, **340**, 123226.
62 D. Tang, J. Li and G. Zhang, A novel open–framework spheniscidite photocatalyst with excellent visible light photocatalytic activity: silver sensitization effect and DFT study, *Appl. Catal. B Environ.*, 2018, **224**, 433–441.
63 L. Jiang, S. Ni, G. Liu and X. Xu, Photocatalytic hydrogen production over Aurivillius compound Bi_3TiNbO_9 and its modifications by Cr/Nb co-doping, *Appl. Catal. B Environ.*, 2017, **217**, 342–352.
64 X. Chen, R. Guo, W. Pan, Y. Yuan, X. Hu, Z. Bi and J. Wang, A novel double S-scheme photocatalyst $Bi_7O_9I_3$/$Cd_{0.5}Zn_{0.5}S$ QDs/WO_{3-x} with efficient full-spectrum-induced phenol photodegradation, *Appl. Catal. B Environ.*, 2022, **318**, 121839.
65 H. Xie, K. Wang, D. Xiang, S. Li and Z. Jin, Enwrapping graphdiyne (g-C_nH_{2n-2}) on hollow $NiCo_2O_4$ nanocages derived from a Prussian blue analogue as a p–n heterojunction for highly efficient photocatalytic hydrogen evolution, *J. Mater. Chem. A*, 2023, **11**, 14971–14989.
66 R. Tang, H. Zeng, C. Feng, S. Xiong, L. Li, Z. Zhou, D. Gong, L. Tang and Y. Deng, Twisty C-TiO_2/PCN S-Scheme Heterojunction with Enhanced n→π * Electronic Excitation for Promoted Piezo-Photocatalytic Effect, *Small*, 2023, **19**, 2207636.
67 C. Ouyang, W. Huang, H. Tang, W. Liu, X. Gu, Z. Hong and M. Zhi, Hierarchical MoO_2/$ZnIn_2S_4$ Schottky Heterojunction Stimulated Photocatalytic H_2 Evolution under Visible Light, *ACS Appl. Energy Mater.*, 2022, **5**, 12739–12751.

 This journal is © The Royal Society of Chemistry 2024